AD-A071 323 UTAH STATE UNIV LOGAN SPACE SCIENCE LAB F/G 4/1
ROCKET MEASUREMENTS OF AURORAL ELECTRON DENSITY IRREGULARITIES --ETC(U)
AUG 78 K D BAKER, J C ULWICK, M C KELLEY DNA001-76-C-0256
UNCLASSIFIED DNA-4676T NL

1 OF 1
AD A071323

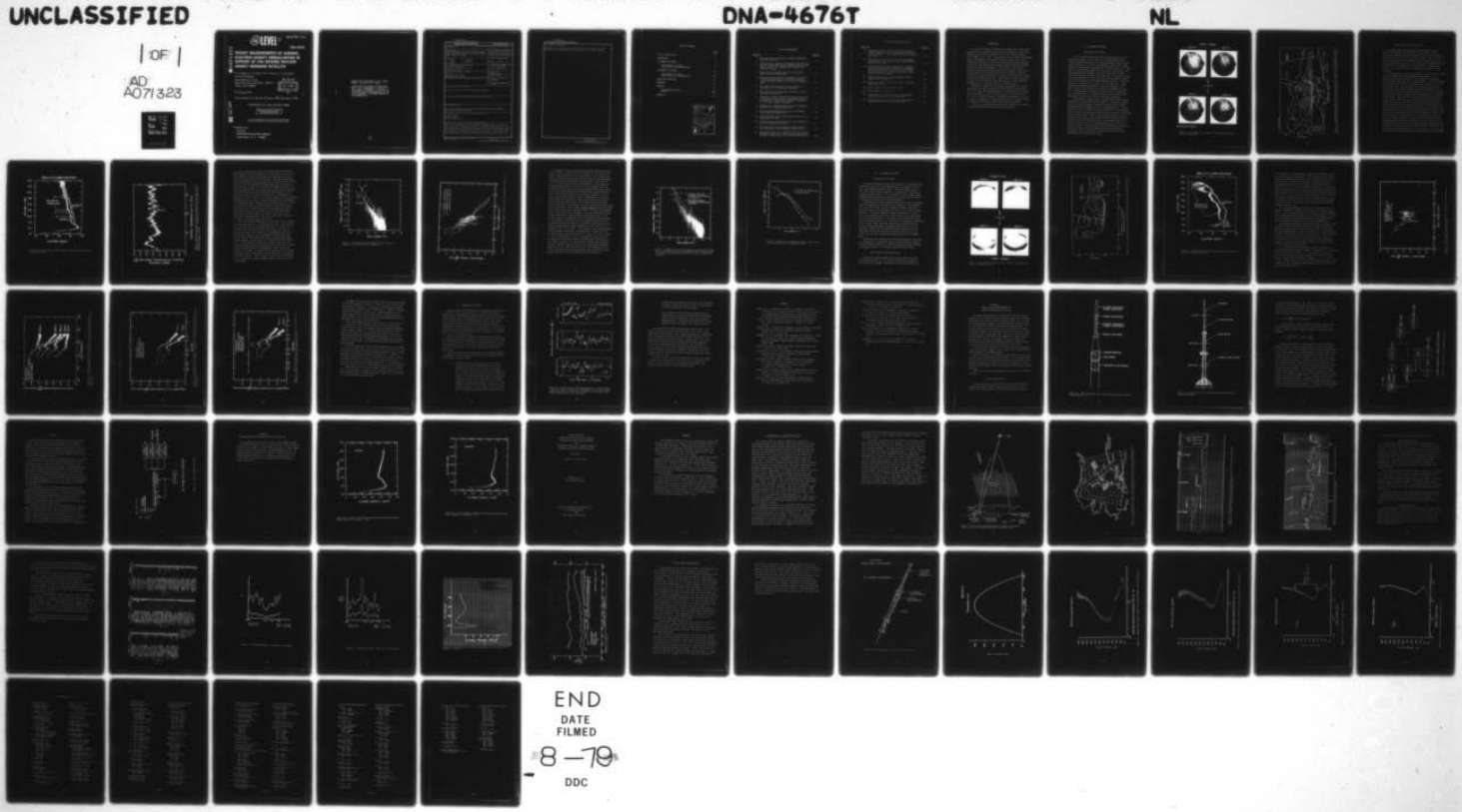

END
DATE FILMED
8-79
DDC

(12) LEVEL III

DNA 4676T

ROCKET MEASUREMENTS OF AURORAL ELECTRON DENSITY IRREGULARITIES IN SUPPORT OF THE DEFENSE NUCLEAR AGENCY WIDEBAND SATELLITE

K. D. Baker, J. C. Ulwick, M. C. Kelley, L. C. Howlett, and N. Grossbard

Utah State University
Space Science Laboratory, UMC-41
Logan, Utah 84322

31 August 1978

Topical Report for Period 15 March 1976—31 August 1978

CONTRACT No. DNA 001-76-C-0256

APPROVED FOR PUBLIC RELEASE;
DISTRIBUTION UNLIMITED.

THIS WORK SPONSORED BY THE DEFENSE NUCLEAR AGENCY
UNDER RDT&E RMSS CODE B322076462 L25AAXHX63320 H2590D.

Prepared for
Director
DEFENSE NUCLEAR AGENCY
Washington, D. C. 20305

Destroy this report when it is no longer needed. Do not return to sender.

PLEASE NOTIFY THE DEFENSE NUCLEAR AGENCY, ATTN: TISI, WASHINGTON, D.C. 20305, IF YOUR ADDRESS IS INCORRECT, IF YOU WISH TO BE DELETED FROM THE DISTRIBUTION LIST, OR IF THE ADDRESSEE IS NO LONGER EMPLOYED BY YOUR ORGANIZATION.

UNCLASSIFIED

SECURITY CLASSIFICATION OF THIS PAGE *(When Data Entered)*

REPORT DOCUMENTATION PAGE		READ INSTRUCTIONS BEFORE COMPLETING FORM
1. REPORT NUMBER DNA 4676T	2. GOVT ACCESSION NO.	3. RECIPIENT'S CATALOG NUMBER
4. TITLE *(and Subtitle)* ROCKET MEASUREMENTS OF AURORAL ELECTRON DENSITY IRREGULARITIES IN SUPPORT OF THE DEFENSE NUCLEAR AGENCY WIDEBAND SATELLITE		5. TYPE OF REPORT & PERIOD COVERED Topical Report for Period 15 March 1976—31 August 1978 6. PERFORMING ORG. REPORT NUMBER
7. AUTHOR(s) K. D. Baker L. C. Howlett J. C. Ulwick N. Grossbard M. C. Kelley		8. CONTRACT OR GRANT NUMBER(s) DNA 001-76-C-0256
9. PERFORMING ORGANIZATION NAME AND ADDRESS Utah State University Space Science Laboratory, UMC-41 Logan, Utah 84322		10. PROGRAM ELEMENT, PROJECT, TASK AREA & WORK UNIT NUMBERS Subtask L25AAXHX633-20
11. CONTROLLING OFFICE NAME AND ADDRESS Director Defense Nuclear Agency Washington, D.C. 20305		12. REPORT DATE 31 August 1978 13. NUMBER OF PAGES 74
14. MONITORING AGENCY NAME & ADDRESS*(if different from Controlling Office)*		15. SECURITY CLASS *(of this report)* UNCLASSIFIED 15a. DECLASSIFICATION/DOWNGRADING SCHEDULE

16. DISTRIBUTION STATEMENT *(of this Report)*

Approved for public release; distribution unlimited.

17. DISTRIBUTION STATEMENT *(of the abstract entered in Block 20, if different from Report)*

18. SUPPLEMENTARY NOTES

This work sponsored by the Defense Nuclear Agency under RDT&E RMSS Code B322076462 L25AAXHX63320 H2590D.

19. KEY WORDS *(Continue on reverse side if necessary and identify by block number)*

Auroral Research
Electron Density
Plasma Irregularities

20. ABSTRACT *(Continue on reverse side if necessary and identify by block number)*

In situ measurements of electron density irregularities in the auroral E and F regions were conducted in support of the DNA Wideband satellite. The results from the two rocket probes that were flown in conjunction with night-time overpasses of the satellite are reported in detail. Significant regions of irregular plasma density fluctuations were detected on both flights, but with somewhat different character and over different spatial regions. The

DD FORM 1 JAN 73 1473 EDITION OF 1 NOV 65 IS OBSOLETE

UNCLASSIFIED

SECURITY CLASSIFICATION OF THIS PAGE *(When Data Entered)*

20. ABSTRACT (Continued)

spectra of the irregularities indicate that they are formed by different mechanisms than those observed in both spread F and in barium clouds.

TABLE OF CONTENTS

LIST OF ILLUSTRATIONS

LIST OF ILLUSTRATIONS (cont.)

INTRODUCTION

A wealth of information concerning the phenomenology of equatorial and auroral scintillation has accrued from the successful flight of the DNA/SRI Wideband satellite [Fremouw, et al., 1977; Rino and Fremouw, 1977; Fremouw, et al., 1978]. The emergence of the new data has encouraged further developments in the theory of scintillations. These studies together with the further results of Wideband satellite and correlative ground-based measurements show progress has begun toward understanding questions of physical mechanisms. In this report we describe the results of three rocket flights which probed the auroral plasma nearly simultaneously with a near overhead pass of the Wideband satellite. At this time detailed information is available only from the two rockets fired in the midnight time period. (The third was launched during the morning of March 1978 and the data tapes are not yet quite completely de-bugged due to an inordinate amount of telemetry noise.)

Nonetheless, significant new insights are apparent from the midnight series and, when put together with the daytime flight in March 1978, will yield a much improved model for the naturally scintillating auroral environment. Since the rockets WS 614-51-3 (11/13/76) and WS 614-51-4 (11/26/76) probed quite different environments, we can use the results to advantage in interpreting the effects of auroral particle precipitation and electric fields on the transmitting medium.

Details of the experimental apparatus are presented in an Appendix along with preliminary results from the daytime flight.

II. 13 NOVEMBER 1978 EVENT

Description of the Event

In the 13 November 1976 flight (51-3), the ionosphere over the Alaskan sector prior to the event could be characterized as background undisturbed conditions. The Chatanika radar reported low peak electron densities $\lesssim 3 \times 10^4$ for the preceding several hours. Superimposed on this quiescent background was an impulse onset of hot plasma injection from the magnetosphere as can be seen in the sequence of all sky photos presented in Figure 1 which were taken from Ft. Yukon about 180 km north of the Poker Flat launch site. The quality of these pictures was degraded by a thin cloud cover, but the sharply defined arc is clearly seen to surge northward extremely rapidly. It has been shown that such surges are not due to electric fields, but to some disturbance propagating through the source region [Kelley, et al., 1971]. Thus at a given point in the region the ionospheric effects were a direct measure of the impulse response to the hot plasma and not a cumulative effect of ionospheric plasma carried along by $\bar{E}x\bar{B}$ drifts with the flux tube on which the hot plasma originated.

Electron density contours from an elevation scan of the Chatanika radar gives further insight into the event as is displayed in Figure 2 along with the total electron content (TEC) deduced from the phase measurement from the Wideband satellite L band transmitter. The slow increase in TEC to the north is a phase trend which is an instrumental effect and had not yet been removed when this plot was made. The intense density contour labeled A and the sharp TEC rise labeled C are both indicative of the first contact between Chatanika and the satellite lines of sight with the poleward surge. The southern portion of the elevation scan and the rest of the wideband pass, then, were both probing a region of recently injected particle precipitation along with the rocket, which was also launched into this recently perturbed environment. We now describe the rocket data and relate it to the Wideband satellite and Chatanika results.

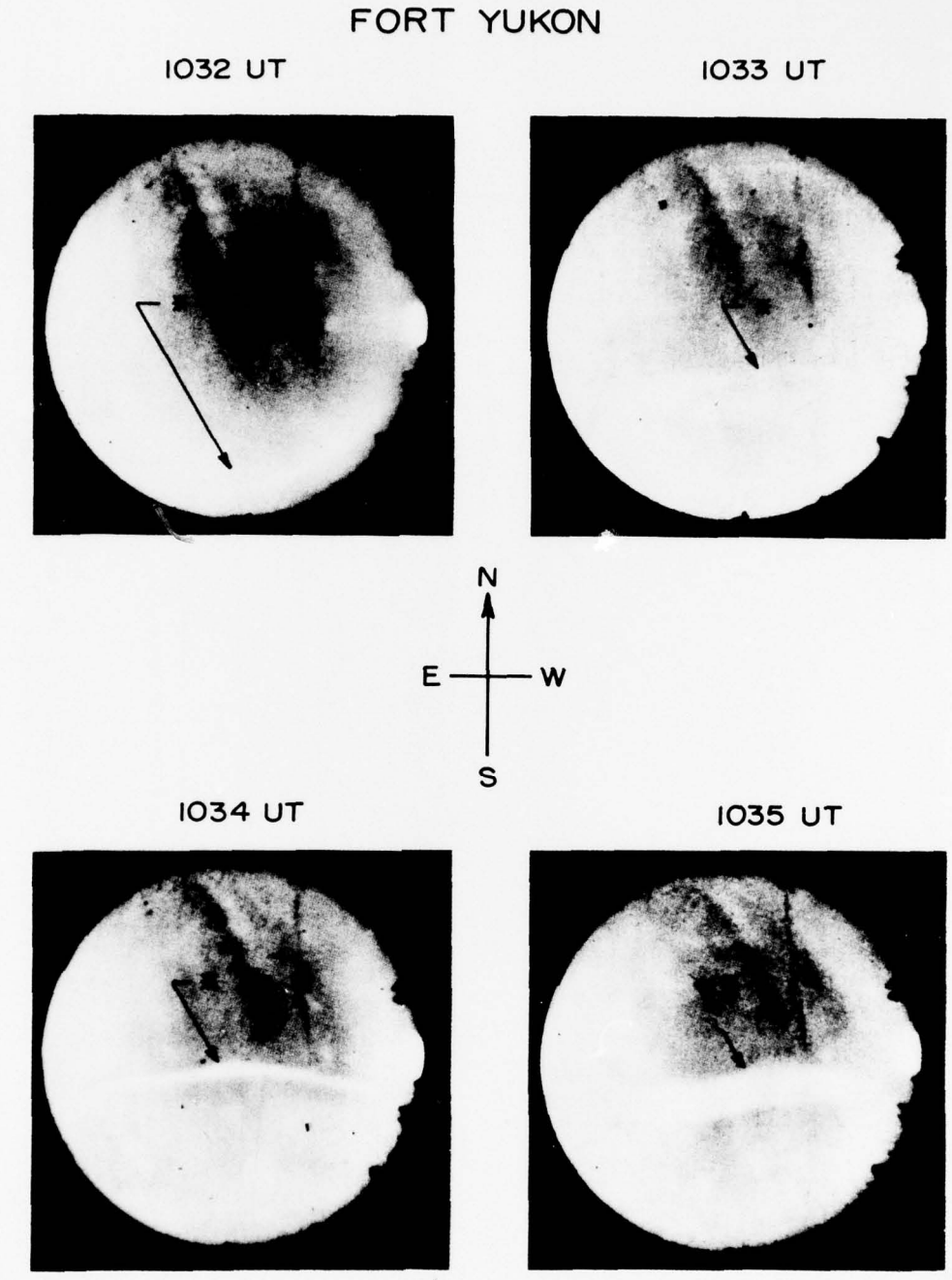

Figure 1. Fort Yukon all sky camera for 13 November 1976 during flight of rocket 51-3.

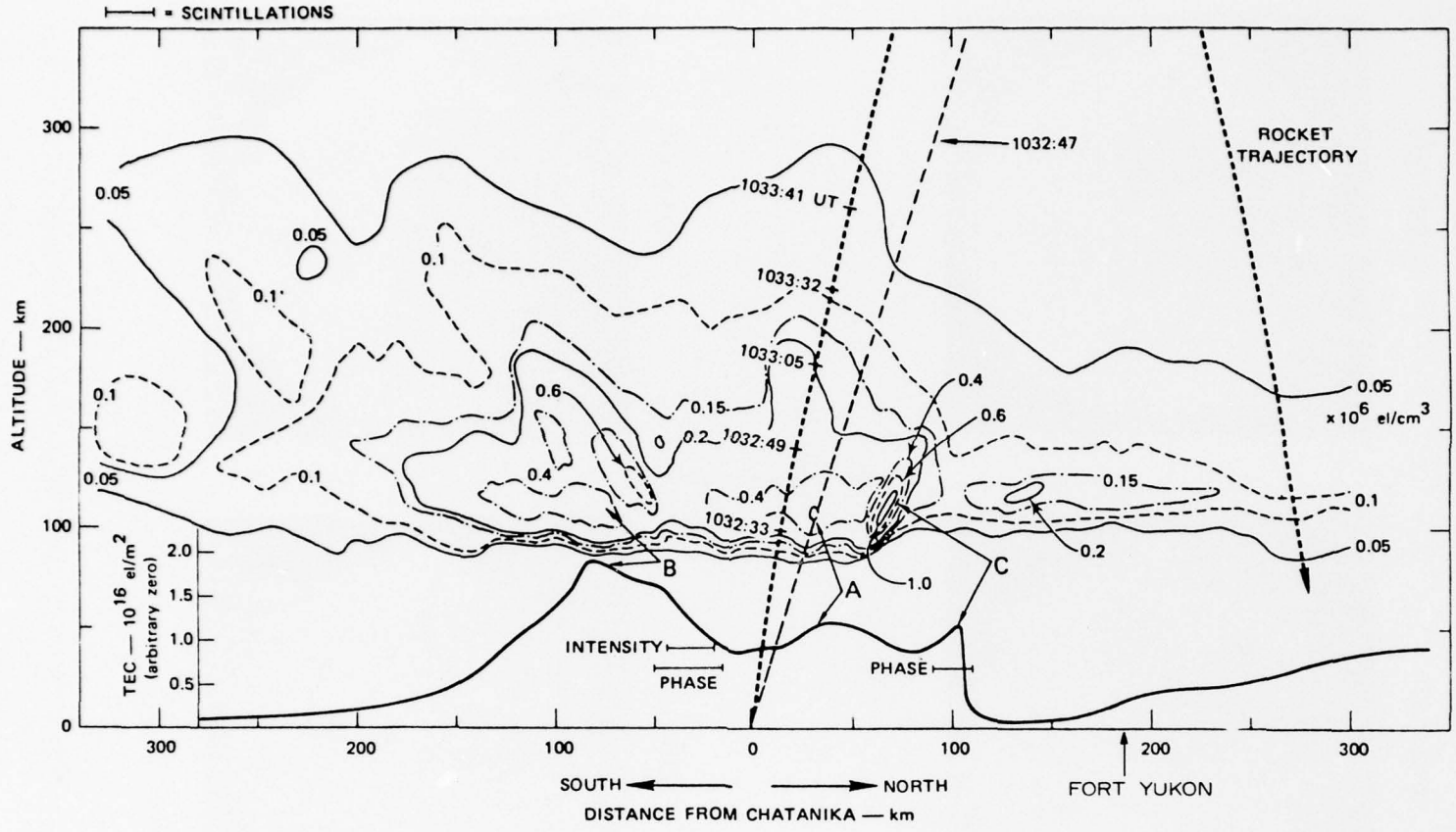

Figure 2. Electron density contours from Chatanika radar and total electron content (TEC) from the Wideband satellite pass during the event of 13 November 1976. Rocket 51-3 trajectory is shown.

Rocket Results and Interpretation

The plasma density profiles obtained from rocket WS 614.51-3 flown on 13 November 1976 at 1031:30 UT are presented in Figure 3. Both ascent and descent profiles developed an E-region electron density profile with a peak of about 5×10^5 electrons/cm^3. This is a factor of about 10 increase over the measured value (Chatanika radar) prior to the hot plasma injection event. The induced density enhancements obvious in these layers in the wake of the poleward surge are another manifestation of the intense particle precipitation associated with the phenomenon.

Two perturbations in electron density over what would be the average level were observed at about 190 km and 240 km altitude. Above 250 km the rocket entered a region of very structured plasma which persisted until about 350 km on the rocket downleg. It is very tempting to associate the two relative perturbations with features A and C on the Chatanika scan. To investigate this possible correlation, the upleg results were examined by detrending the data between 152 km and 450 km and by fitting a polynomial of degree 1 to the log of the density versus altitude, thereby approximating the exponential decay exhibited in the profile. Each data point was then divided by the value of the fitting curve at that point to yield a running value for the relative density variations ($\Delta n/n$). This is the most straightforward way to remove the normal altitude variation in the data. Figure 4 shows the $\Delta n/n$ data plotted versus "distance" perpendicular to the magnetic field. Quotation marks are used since we have taken the mean component of rocket velocity perpendicular to $\bar{B}$ in the time period which yields a qualitatively correct presentation since the perpendicular velocity does not vary too much on the upleg. Note that we have corrected for the mean equatorward velocity of the plasma as a whole as deduced from the Chatanika line of sight drift measurements during the flight (provided by M. Baron of SRI International). About 25 km has to be added to get the total range from the launch site. The double peak at the beginning of the data set corresponds roughly with the feature A in the Chatanika

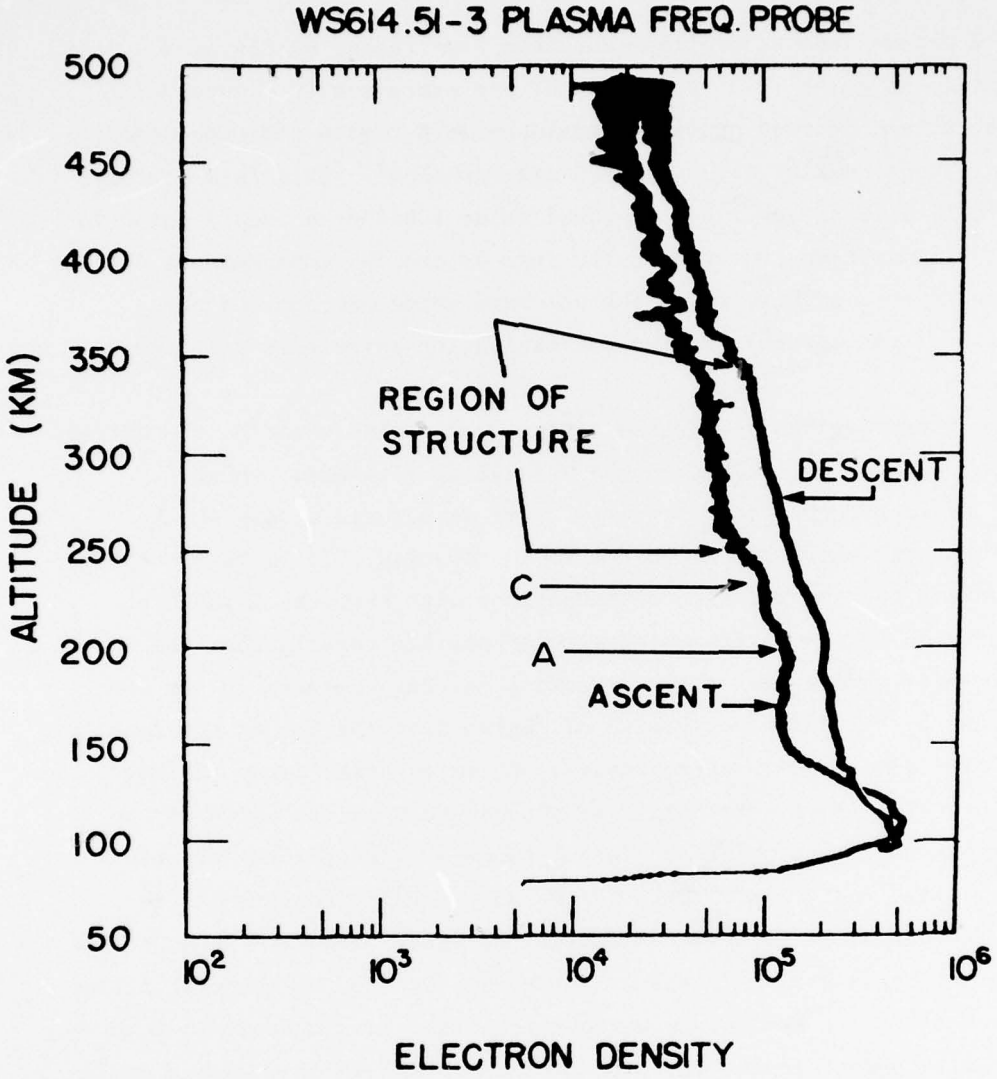

Figure 3. Electron density profiles measured by probe rocket WS614.51-3 on 13 November 1976.

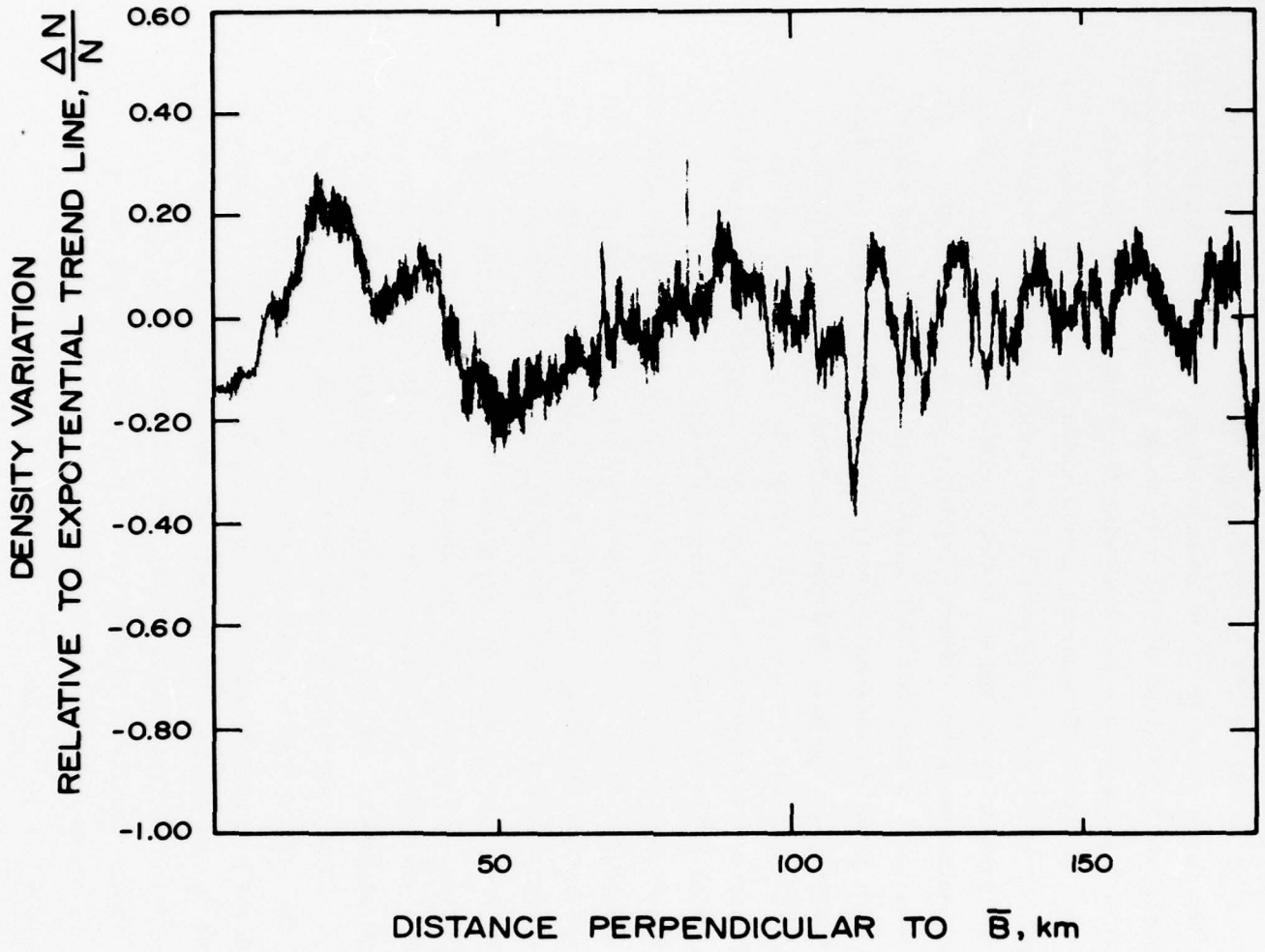

Figure 4. Detrended electron density data (Rocket 51-3) from 152 to 450 km (ascent) shown as a function of distance travelled by rocket normal to the terrestrial magnetic field.

scan and the increase near 90 km to the north (feature C) observed by both Chatanika and the TEC techniques. Extrapolation from the rest of the Chatanika scan yields another relative perturbation in electron density some 50 km south of the launch site. Although not definitive, these data suggest that the outer scale for auroral scintillation structures may be in the 50-100 km wavelength regime which is indeed well above the range of scale sizes associated with VHF scintillation. The wave number power spectrum of the data shown in Figure 4 is reproduced in Figure 5 along with a curve showing the slope expected for a k^{-2} power law spectrum. To convert from frequency ω to wavenumber k, we assumed $k = \omega/(V_1 + V_c)$ where V_1 is the mean component of rocket velocity perperpendicular to B, and V_c the equatorward plasma velocity measured by the Chatanika radar. Several features are worth discussing. There does seem to be a peak for $\lambda \approx 50$ km although the very lowest spatial scale data point is extremely sensitive to the detrending technique. Such analyses are usually discussed in terms of power law indices. Viewed this way there seems to be a break in the "slope" of the curve near a wave number of $k_n \approx 1$ km^{-1} with roughly a k^{-2} form below k_n and with a flatter spectral form above k_n.

Since this analysis emphasized the largest scale sizes available from the rocket data set, it included both the lower, smooth region of the profile and the more structured region above. To study this in more detail the data set was divided into shorter time intervals and the same type of analysis applied. Representative power spectra are plotted in Figure 6. In the important wave number regime from 0.4 to 1 km^{-1} there was indeed more power in the structured regime at high altitude. One must take care in interpreting this, however, since it is the absolute fluctuations in density which cause scintillation effects and not the relative density plotted here. We have listed the electron density corresponding to each of the spectra plotted in the legend. To "normalize" the power spectra with respect to absolute electron fluctuations, one must multiply by the square of the absolute density. Treated in this way, the peak at 365 km would still be present, but would be somewhat reduced relative to value at other heights.

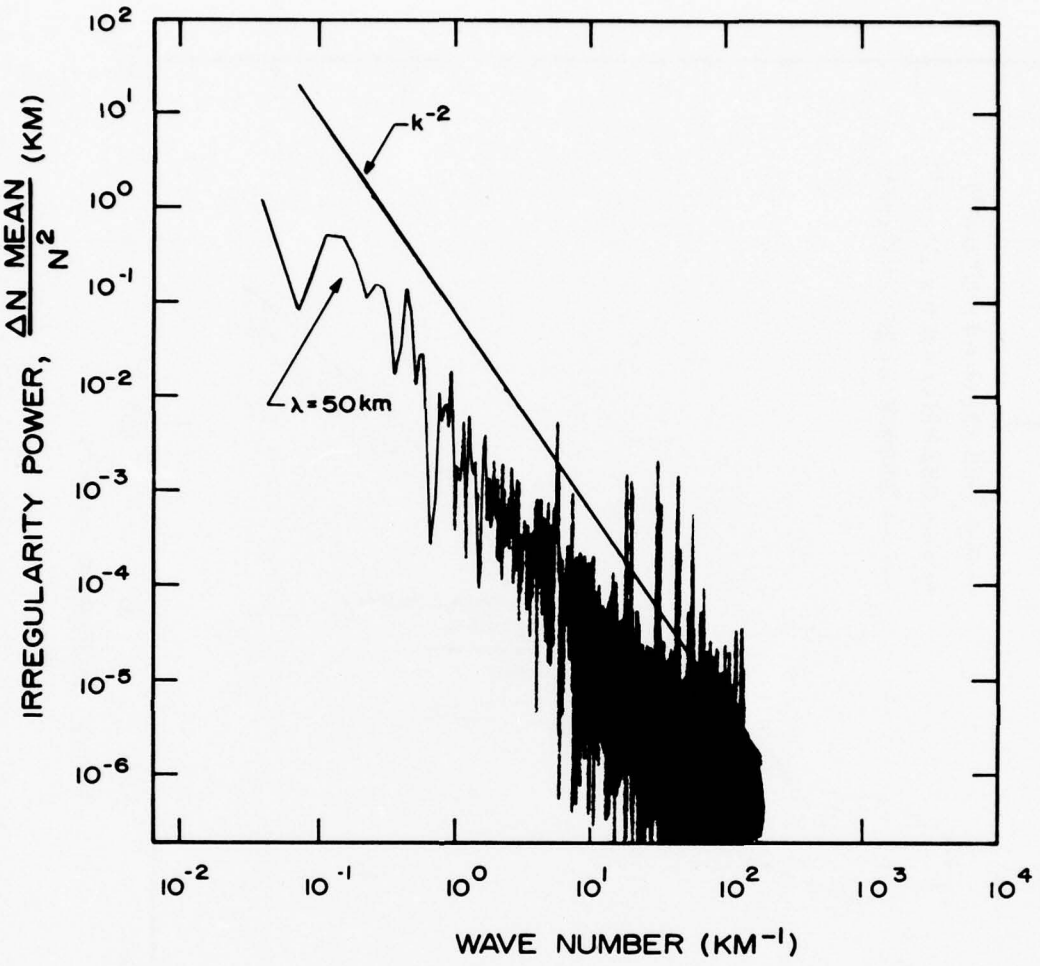

Figure 5. Wave number power spectrum for data of Figure 4. A spectrum for a k^{-2} is shown for comparison.

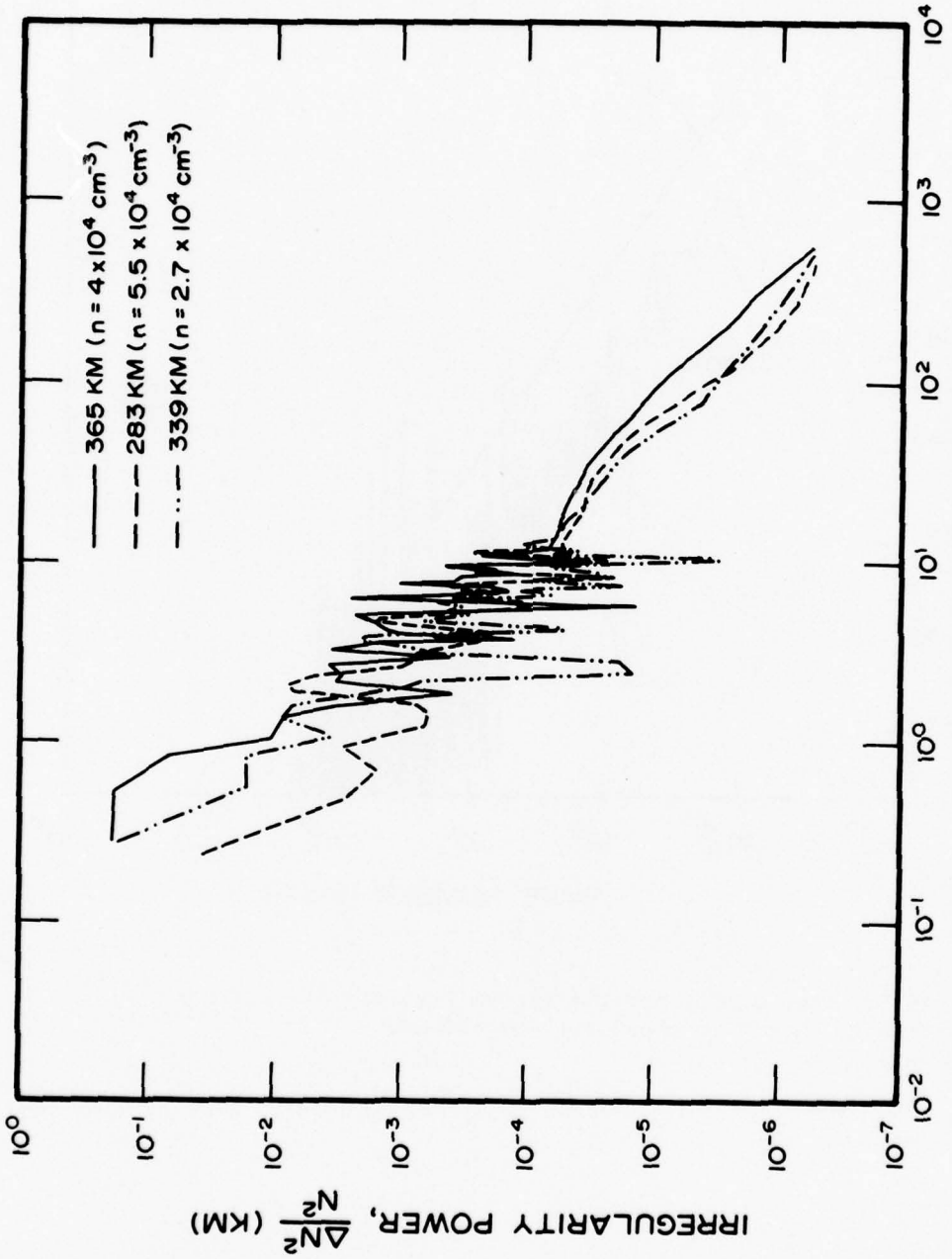

Figure 6. Power spectra of electron density variation for three altitudes of flight 51-3.

We suggest here that the spectrum labeled 365, reproduced in more detail in Figure 7, could be taken as the model for the F-region ionosphere recently subjected to hot plasma injection. The intensity and phase scintillations expected from these fluctuations could be compared to those measured by the Wideband satellite system at about 1034 UT since the region probed then also corresponded to a region perturbed by the same auroral event. Note that it is not surprising that the structured plasma was delayed at rocket altitude ($\sim$1034:45 UT) relative to the particle deposition at low altitudes along the same field line since a finite time (on the order of minutes) is required for the F region to react [Roble and Rees, 1977]. Combining the all sky camera pictures with the trajectory, we found that the discrete arc passed by the 100 km projection along B of the rocket position 136 seconds prior to detection of the structure. We have also plotted the wave number power spectrum from a rocket flight through bottomside equatorial spread F in the same Figure [Costa and Kelley, 1978]. The relative fluctuation power was about the same at the equator as was the background electron density and altitude. Thus the amplitude scintillation due to this structure should be comparable to that of bottomside equatorial spread F. This seems to be the case in both the Wideband satellite data of 13 November 1976 and the equatorial scintillation levels during strictly bottomside events [Basu, private communication, 1977] where S_4 is in the range of 0.1 to 0.4 at VHF. It is important to note that the spread F power spectrum is more nearly characterized by a single index than the auroral data. The former lies near -2.1, while the latter is closer to -3 for $0.1 \leq k \leq 4$ and to -1 for $k > 4$. The equatorial power spectrum is compared to measurements inside a striated barium cloud during project STRESS in Figure 8. The two agree in both amplitude and spectral form which strongly suggests that the linear and nonlinear formation mechanisms are very similar [Kelley, et al., 1978; Scannapieco, et al., 1976]. The differences between the auroral case and the barium cloud/equatorial spread F case are discussed in more detail later.

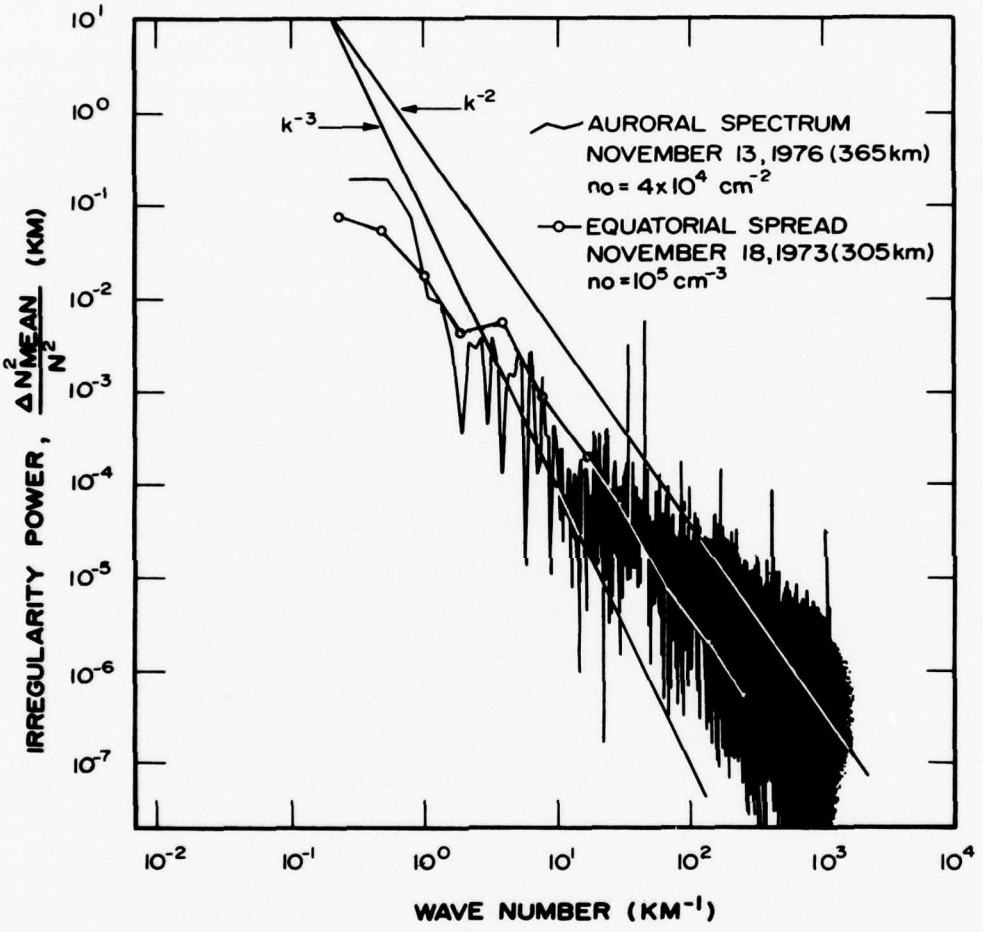

Figure 7. Comparison of auroral irregularity spectrum from flight 51-3 at 365 km with spectrum of equatorial spread-F irregularities. Simple power law spectra with indices of -2 and -3 are shown for reference.

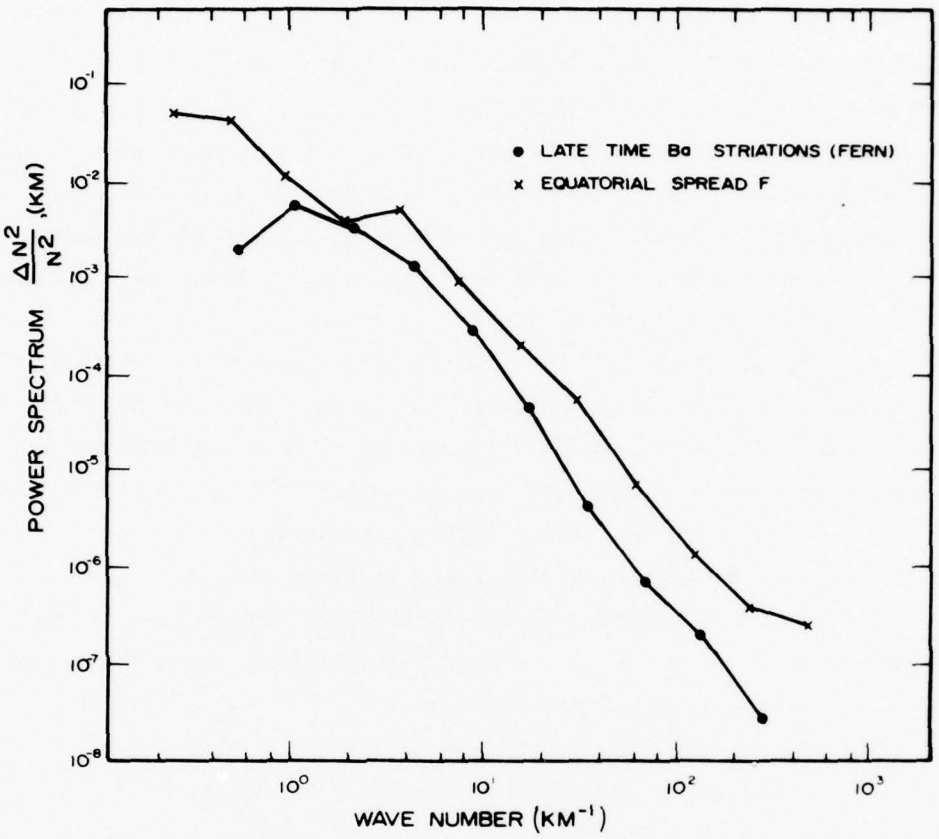

Figure 8. Comparison of irregularity spectra found in equatorial spread-F and a striated barium cloud.

III. 26 NOVEMBER 1976 EVENT

Description of the Event

The auroral environment during Rocket Flight 51-4 (26 November 1976, 1025:40 UT) was that of a post break-up aurora. A sequence of all sky camera photographs presented in Figure 9 show that discrete and diffuse auroral features were present for a long period of time and over a large latitudinal extent. Thus the sources of auroral plasma density enhancement were present for a long period of time as were the electric fields associated with discrete auroral structures.

Electron density contours from the elevation scan from the Chatanika radar are reproduced in the lower portion of Figure 10. The northernmost of the two distinct, aurorally enhanced E regions corresponds to the discrete arc on the right-hand side of the Ft. Yukon all sky photos (Figure 9). The broader enhanced E region corresponds to the broad arc on the left-hand side of the Ft. Yukon pictures and the right-hand side of the Poker Flat photos. This pass has been extensively studied by the SRI group [Fremouw, et al., 1977] due to strong phase scintillation, and to a lesser extent, amplitude scintillation associated with the F region feature equatorward of Chatanika and displayed in the upper two panels. Modest phase and amplitude scintillations were seen in conjunction with the two discrete arcs which are similar to, albeit weaker than, the phase scintillations associated with the 13 November event.

The SRI group has interpreted the observed disturbance as being due to a combination of a geometrical effect from the east-west elongation of enhanced density regions and a possible additional irregular feature of the medium related to the poleward edge of the plasma trough.

Rocket Results and Interpretation

The upleg and downleg plasma density profiles from rocket 51-4 are presented in Figure 11. An intense E-region layer was detected on rocket ascent, presumably corresponding to the visual auroral arcs

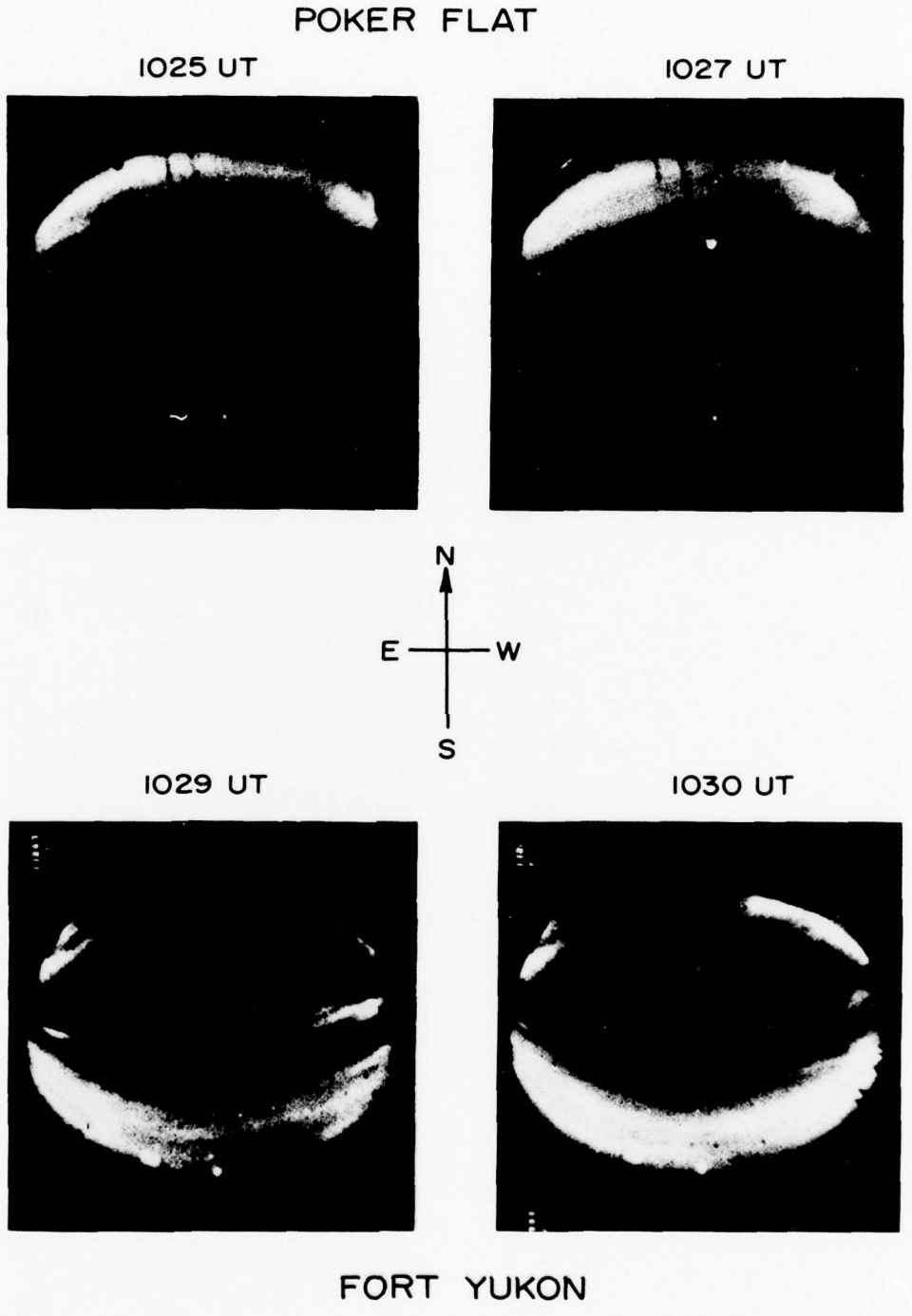

Figure 9. All sky camera pictures for the event of 26 November 1976 (Rocket Flight WS614.51-4).

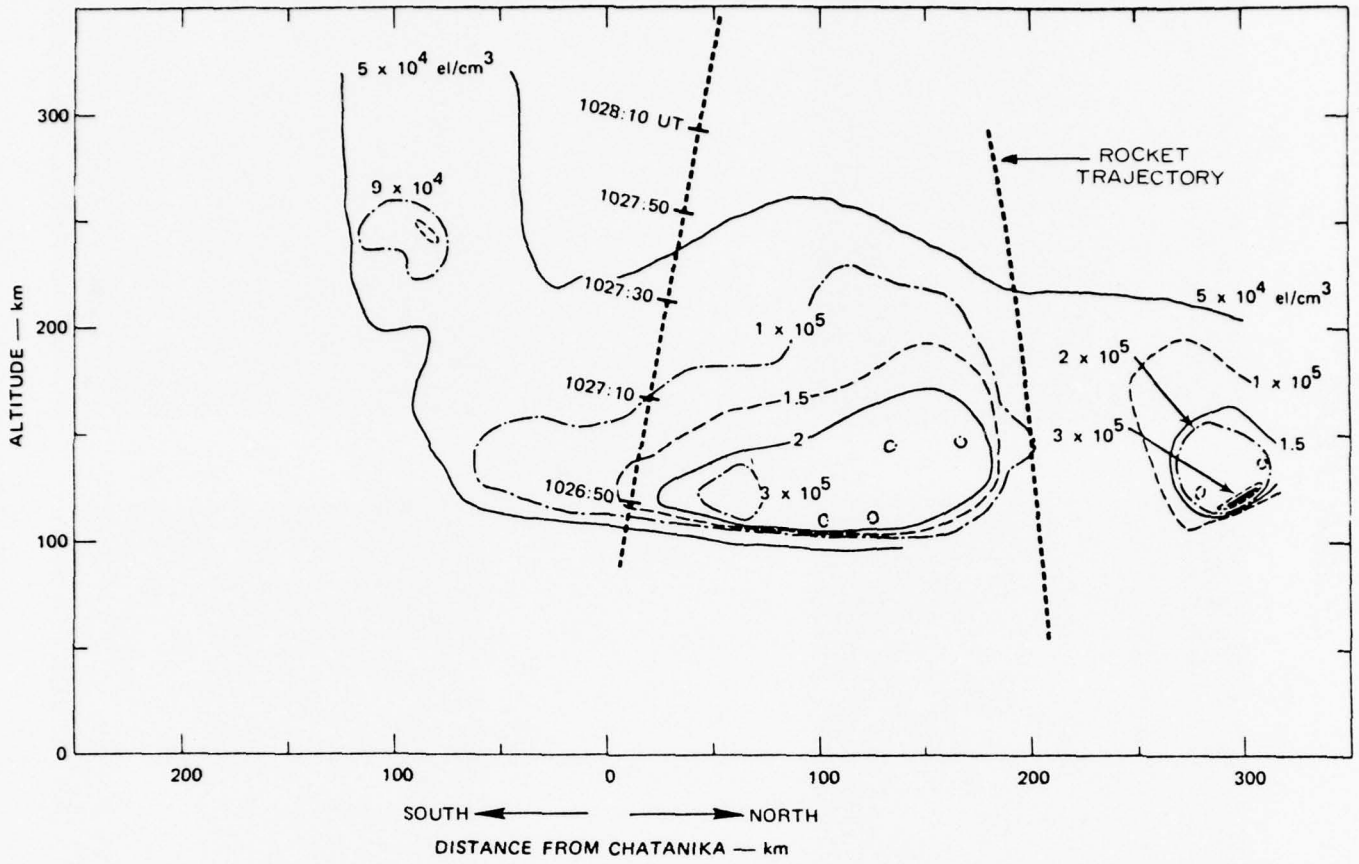

Figure 10. Electron density contours from Chatanika radar for the 26 November 1976 Event.

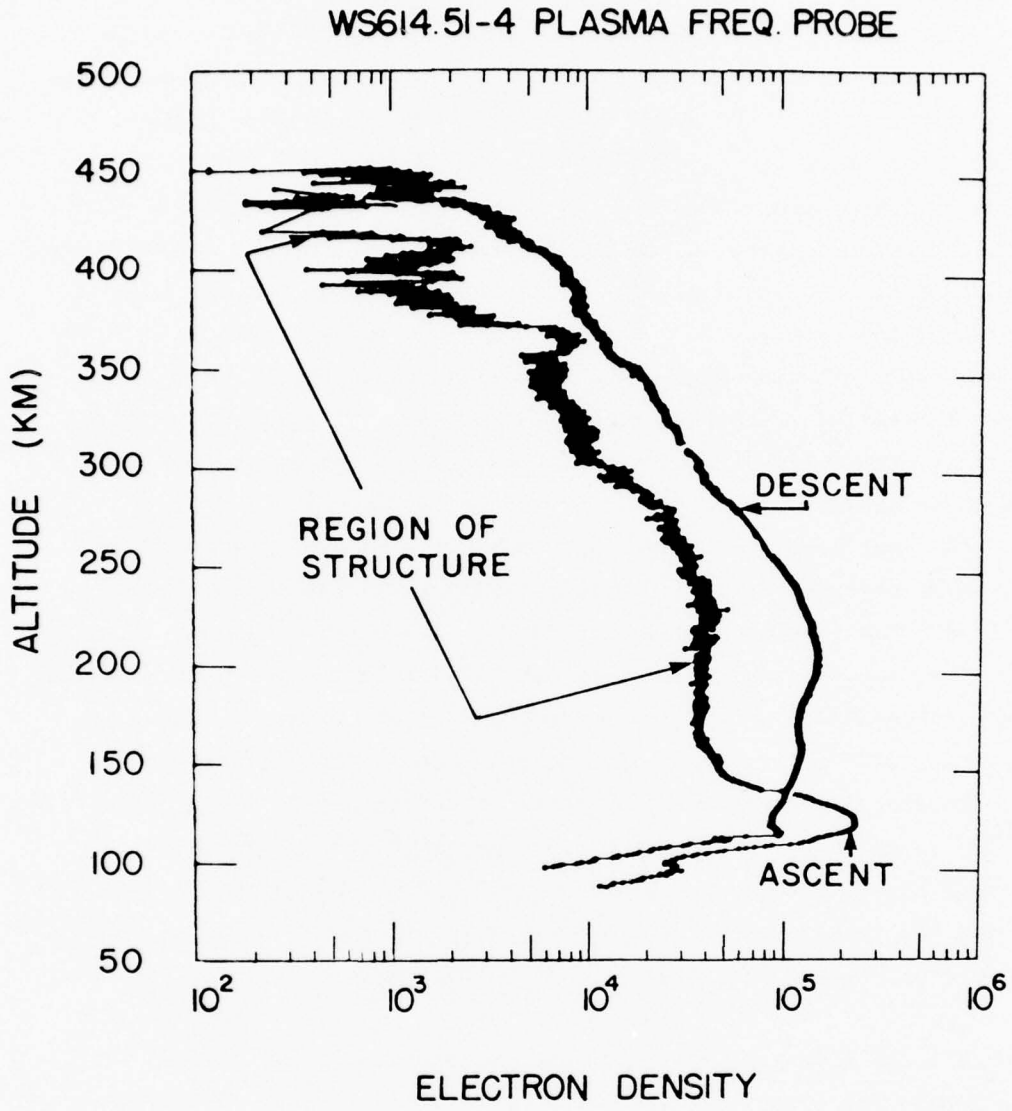

Figure 11. Electron density profiles measured by rocket WS614.51-4 for the 26 November 1976 Event.

in the trajectory. The downleg data showed a well-developed F region, but no distinct low altitude layer. This corresponds to the region of weak auroral emissions between the two arcs as most easily seen in the Ft. Yukon photos. Very sharp fluctuations of plasma density were encountered above 350 km on rocket upleg. When mapped along the magnetic field line to 110 km, and within the accuracy of the scaling, these structures appear to be related to the most intense auroral light emissions in the center of the banded structure just between Poker Flat and Ft. Yukon (see arrow on the Ft. Yukon photograph taken at 1030 UT). The multiple crossing may be due to the arc boundary motion back and forth across the rocket position rather than as a result of multiple distinct structures. If distinct, however, the typical north-south dimension was about 5 km.

The long wavelength power spectrum for a 24 second period near 250 km is reproduced in Figure 12 as analyzed by the method described earlier. The results are similar to the 51-3 data. Again the downleg data were smoother than the upleg but the density was higher. The low level of amplitude scintillation detected by the wideband system may be due to diffractive scintillation from these irregularities.

Interesting power spectral peaks were detected in the range between 60-100 Hertz during the upleg portion of the flight of rocket 51-4, whereas the same frequency range was relatively free of enhancements during the downleg and in the data from rocket 51-3. This is apparent in Figure 13 where the results of a Fourier analysis of short time intervals near 200, 220, 250, 350, and 450 km are plotted. The scales are relative and the curves have been shifted to allow comparison of features. The curves are very similar in shape with the peak moving to lower frequencies at later times.

We can test hypotheses concerning the source of these waves by converting the temporal spectra to spatial by assuming that the frequency and wave number are related by $\omega = kV$. If we choose the velocity V equal to the component of velocity parallel to the Earth's magnetic field, we obtain the representation in Figure 14. This corresponds to $\bar{k} \| \bar{B}$. Assuming $\bar{k} \perp \bar{B}$, as was done in the previous plots in this report, we obtain Figure 15 (again the Chatanika deduced equatorward drift was added to the rocket velocity).

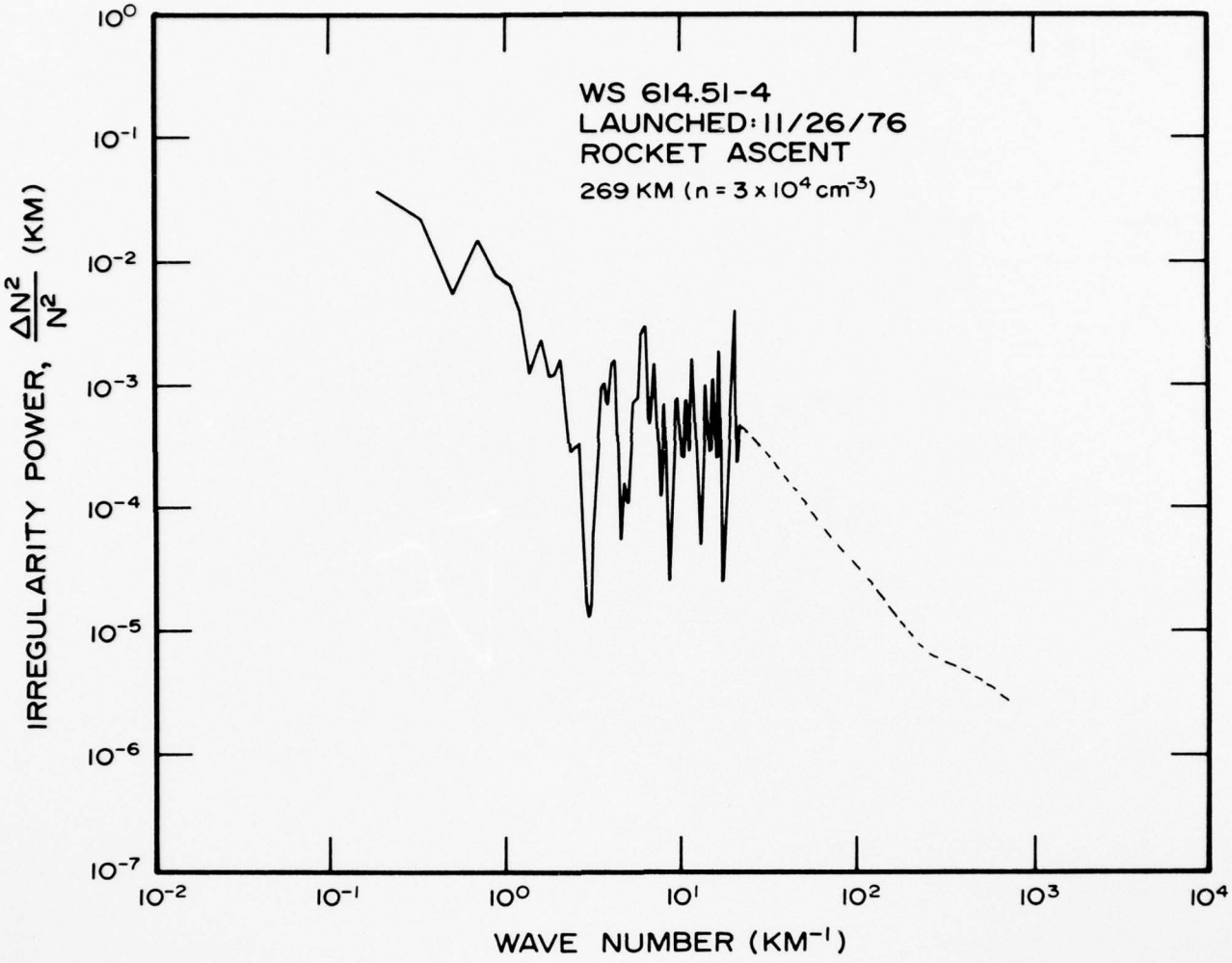

Figure 12. Power spectrum of electron density irregularities for data from rocket 51-4 (26 November 1976) at 269 km.

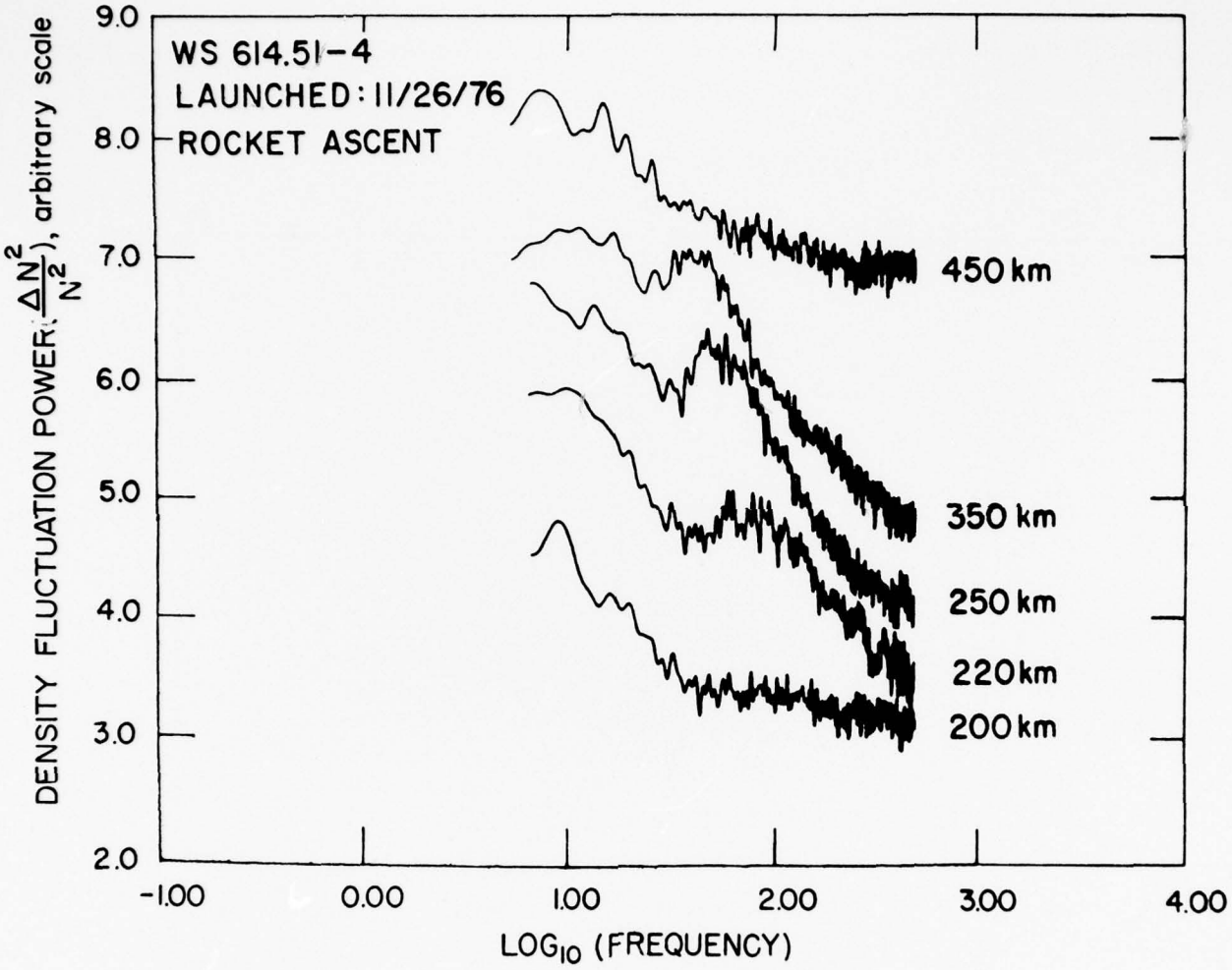

Figure 13. Irregularity spectra (vs. frequency) for five different altitudes of rocket 51-4. The vertical scales are relative only and the curves have been shifted for clarity.

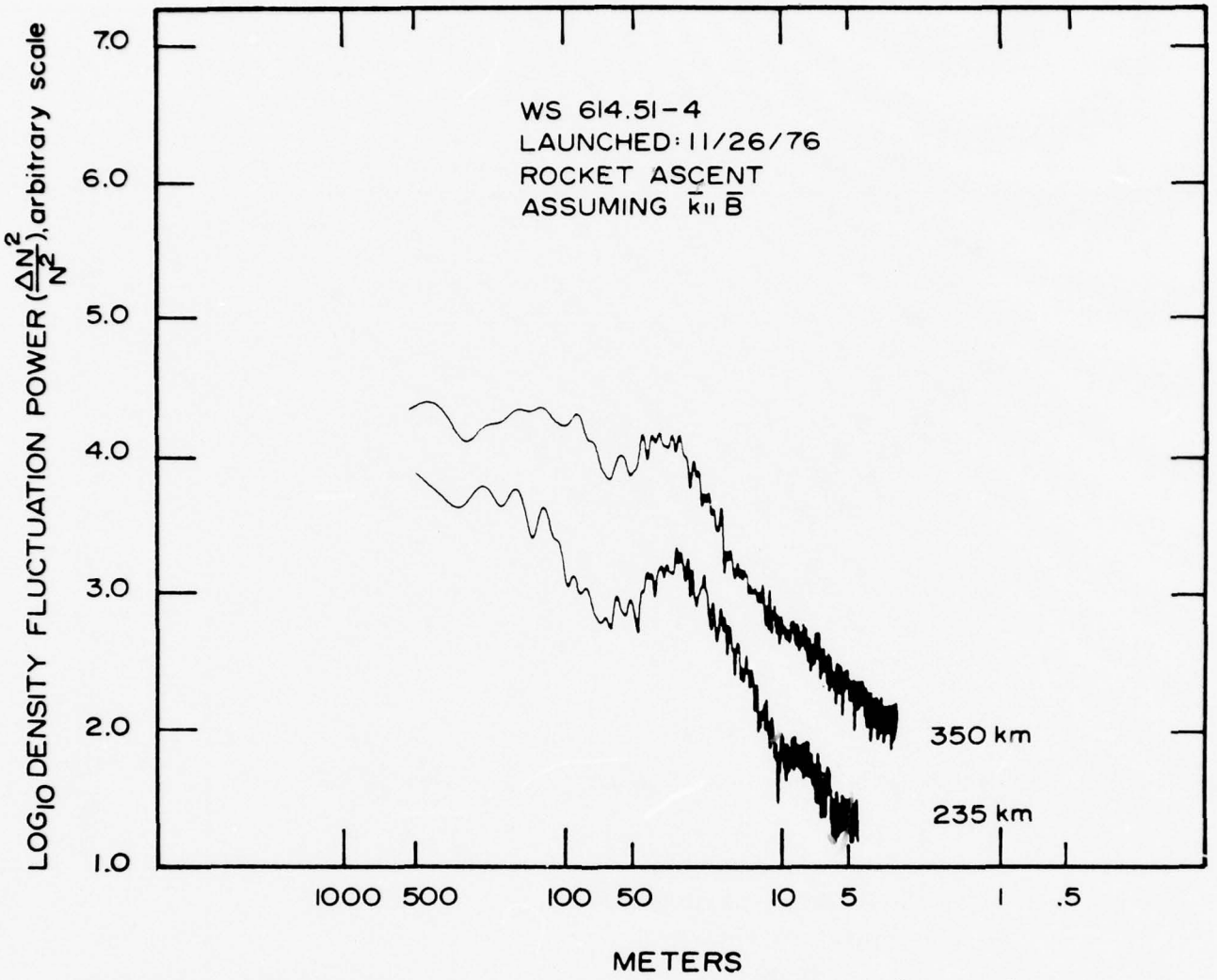

Figure 14. Irregularity spectra versus size obtained using the velocity component along the magnetic field for altitudes of flight 51-3. The curves are shifted vertically for clarity.

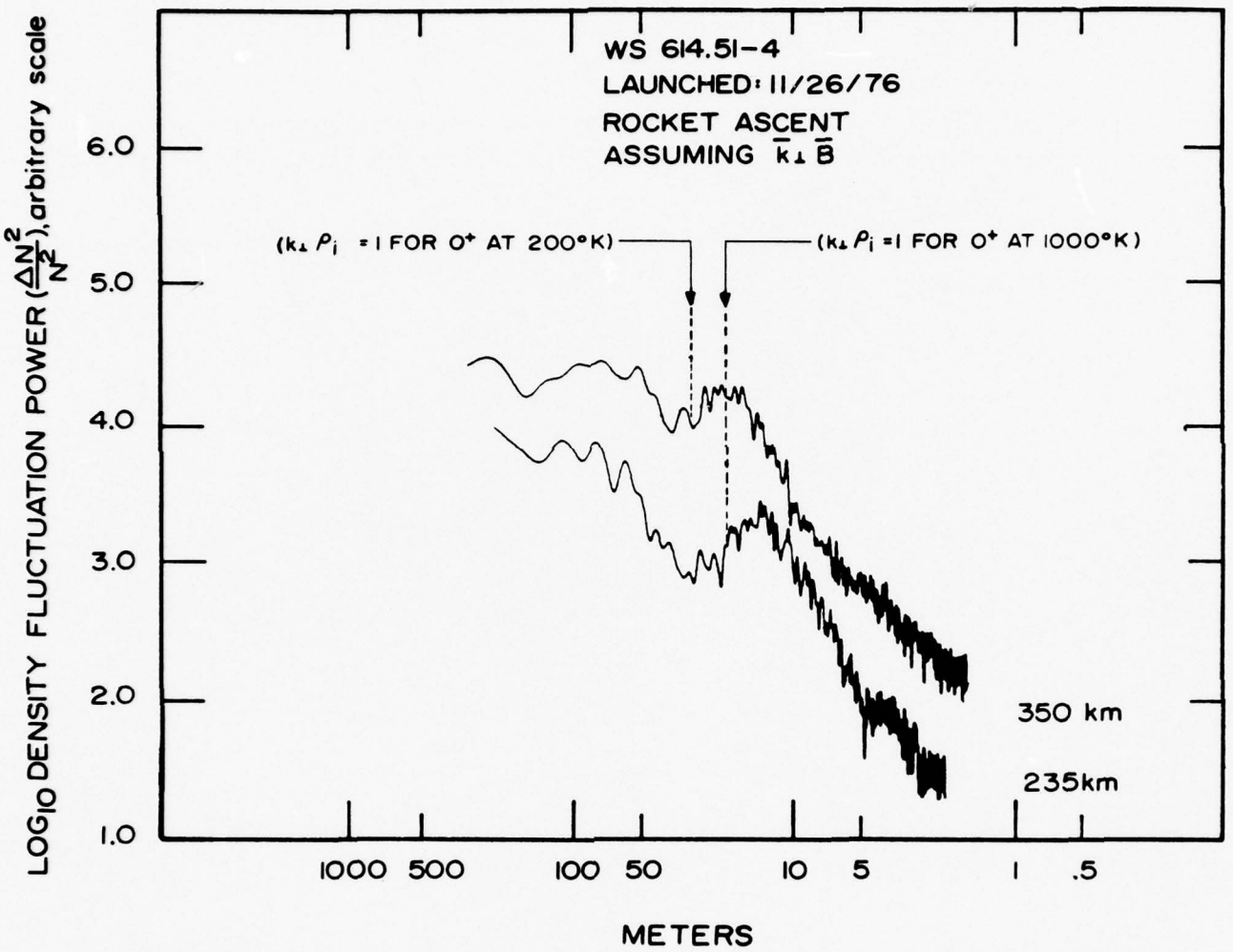

Figure 15. Same data as Figure 14 except the velocity component perpendicular to the magnetic field is used to obtain the horizontal scale.

The peaks in the spatial power spectra seem to line up more closely for the $\bar{k}||\bar{B}$ assumption. However, in Figure 15 we have identified the wave number for which $k_\perp \rho_i = 1$, where ρ_i is the oxygen ion gyroradius, at two different temperatures ($T_i = 1000^\circ K$ and $T_i = 2000^\circ K$). The higher altitude ions might be expected to have a higher temperature due to auroral heating and due to the cooling effect of neutral molecules at lower altitudes. Thus, we cannot rule out either mechanism in this way and hence, will discuss both possibilities.

The possible identification of waves with $k_\perp \rho_i = 1$ leads naturally to a suggestion of ion cyclotron waves driven by the field-aligned currents known to exist in conjunction with the sharp density gradients clearly evident in Figure 11. Electric field observations of waves of both of these types were reported from earlier auroral zone rocket experiments covering the same wavelength range [Kelley, et al., 1975; Kelley and Carlson, 1977]. Observations of irregularities equatorward of the arc could be due to the equatorward plasma drift reported by the Chatanika radar.

If $\bar{k}||\bar{B}$ is appropriate, the most likely explanation of the phenomena involves ion acoustic waves. These waves have been detected in the solar wind [Gurnett and Frank, 1978] and in active ionospheric chemical release experiments involving ion-ion streaming [Kintner, et al., 1978], but displayed a peak density at $\lambda/\lambda d \approx 5$, where λd is Debye length. The peak wavelength in Figure 15 corresponds to $\lambda/\lambda d \lesssim 1000$. This could be reconciled if the waves are travelling parallel to the rocket motions at nearly the same phase velocity, hence downshifting the detected frequency.

Simultaneous electric field and density fluctuations are necessary to solve this dilemma. It should be noted that peaked spectra at $\lambda \lesssim 1m$ were detected during the STRESS rocket flights [Baker, et al., 1977] and also have defied definitive explanation.

IV. SUMMARY AND DISCUSSION

Significant phase scintillation events were observed during these nights without strong amplitude effects. The rocket data support arguments based on Chatanika and Wideband satellite data that ionization layers caused by particle precipitation in the E and F layer contribute to these phase effects. The identification of density enhancements embedded within broad auroral emissions with intense banded light enhancements stretching across the sky also argues for the "onion skin" description of auroral structures. One interpretation of the data from rocket 51-4 is that several structures only 5 km thick were crossed by the rocket on its northward motion.

Regions of irregular plasma density fluctuations were detected on both flights at power levels comparable to those observed at the equator on the bottomside of the F region peak. Diffractive scatter from these irregularities may be the cause of the low level VHF amplitude scintillations at the level of S_4 = 0.1 to 0.4 observed in the nightside auroral oval.

There is evidence in the rocket data that the formation mechanism or mechanisms are quite different from both those of equatorial spread F and striations of barium clouds.

1. The waveform for the irregularities as displayed in Figure 4 are much more "turbulence-like" than those observed in both spread F and barium clouds [Kelley, et al., 1978]. The latter seem more like steepened structures as predicted in the nonlinear theory of bottomside spread F. For example, the probe data obtained during a flight through the barium release Fern (in the STRESS program) is plotted in the top panel of Figure 16. The structures display greater tendency for steep edges than do those in Figure 4. Figure 4 data, in fact, look more like the bottom two panels which have an identical power

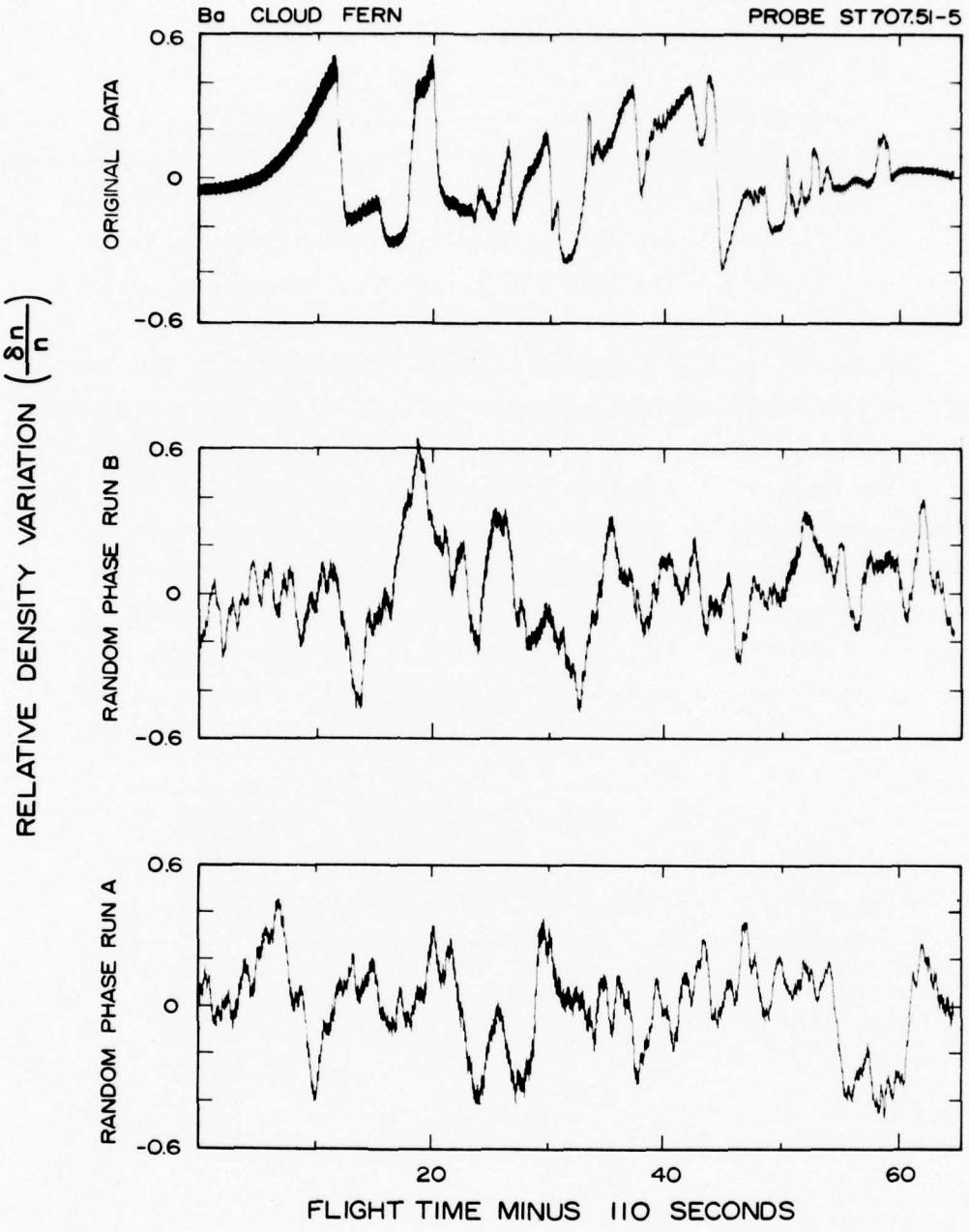

Figure 16. Relative density variations measured in a striated barium cloud (upper panel) compared with "randomized" data created by adding random phase factors to each Fourier component of the original data before reconstruction in the time domain.

spectrum to the top panel, but which have been "randomized" by adding a random phase factor to each Fourier component before reconstruction in the time domain.

2. The irregularities detected during rocket flight 51-3 appeared almost as soon as the plasma density enhancement itself could have propagated to the rocket altitude via thermal expansion. Slow acting instabilities such as the $\bar{E}x\bar{B}$ process thus seem unlikely as a causative process.

Two sources of the irregular plasma density come to mind. First, there is a possible inherent spatial variation in the electron fluxes producing the plasma density. These irregularities would be transported out of the production region by dc electric fields and could fill the volume outside discrete auroral features. Second, there is the action of turbulent electrostatic fields upon horizontal density gradients created by the auroral particle precipitation. Such variations in electric fields are an ubiquitous feature of the auroral zone, polar cap, and sub-auroral zone [Kelley and Mozer, 1972] and have also been invoked in this way to explain the wake structures in equatorial spread F [Kelley and Ott, 1978].

The short wavelength structures observed are not obviously relevant to scintillation studies, but are of interest to the general question of auroral zone irregularities and two-dimensional turbulence and possible "clutter" effects on short wavelength radars.

REFERENCES

Baker, K.D., J.C. Ulwick, M.C. Kelley, L.C. Howlett, G.D. Allred, D. Delorey, and N. Grossbard, *Electron Density Structure in Barium Clouds--Measurements and Interpretation*, Final Report, Contract No. DNA 001-76-C-0278, February 1978, Utah State University.

Costa, E. and M.C. Kelley, On the role of steepened structures and drift waves in equatorial spread F, *J. Geophys. Res.*, 1978, in press.

Fremouw, E.J., C.L. Rino, R.C. Livingston, and M.D. Cousins, A persistent sub-auroral scintillation enhancement observed in Alaska, *Geophys. Res. L.*, *4*(539), 1977.

Fremouw, E.J., R.L. Leadabrand, R.C. Livingston, M.D. Cousins, C.L. Rino, B.C. Fair and R.A. Long, Early results from the DNA Wideband satellite experiment--Complex-signal scintillation, *Radio Science* *13*(167), 1978.

Gurnett, D.A. and L.A. Frank, Ion acoustic waves in the solar wind, *J. Geophys. Res.*, *83*(58), 1978.

Kelley, M.C., J.A. Starr, and F.S. Mozer, Relationship between magnetospheric electric fields and the motion of auroral forms, *J. Geophys. Res.*, *76*(5269), 1971.

Kelley, M.C. and F.S. Mozer, A satellite survey of vector electric fields in the ionosphere at frequencies of 10 to 500 Hertz, 1. Isotropic, high-latitude electrostatic emission, *J. Geophys. Res.*, *77*(4158), 1972.

Kelley, M.C., E.A. Bering, and F.S. Mozer, Evidence that the electrostatic ion cyclotron instability is saturated by ion hating, *The Physics of Fluids*, *18*(1590), 1975.

Kelley, M.C. and C.W. Carlson, Observations of intense velocity shear and associated electrostatic waves near an auroral arc, *J. Geophys. Res.*, *82*(2343), 1977.

Kelley, M.C., K.D. Baker, and J.C. Ulwick, Late time barium cloud striations and their possible relationship to equatorial spread F, *J. Geophys. Res.*, 1978 to be published.

Kelley, M.C. and E. Ott, Two-dimensional turbulence in equatorial spread F, *J. Geophys. Res.*, 1978 to be published.

Kintner, P.M., M.C. Kelley, G. Holmgren and R. Bostrum, *The Observation of Production of Ion Acoustic Waves During the TRIGGER Experiment*, Cornell Report 78-4, 1978.

Rino, C.L. and E.J. Fremouw, The angle dependence of singly scattered wavefields, *J. Atmos. Terr. Phys.*, *39*(859), 1977.

Roble, R.G. and M.H. Rees, Time-dependent studies of the aurora: Effects of particle precipitation on the dynamic morphology of ionospheric and atmospheric properties, *Planet, Space Sci.*, *25*(991), 1977.

Scannapieco, A.J., S.L. Ossakow, S.R. Godman, and J.M. Pierre, Plasma cloud late time striation spectra, *J. Geophys. Res.*, *81*(937), 1976.

APPENDIX A
ROCKET PAYLOADS FOR MEASUREMENT OF AURORAL ELECTRON DENSITY STRUCTURE

The rocket instrumentation for measurement of electron density structure in the auroral ionosphere utilized a 1-meter probe extending forward along the vehicle spin axis as shown in Figure A-1. This general configuration was common to the rocket payloads flown the nights of 13 and 26 November 1976 and the 1 March 1978 daytime flight. The two night flights utilized the probe for an rf antenna for a combination plasma frequency and capacitance probe, while the daytime flight utilized the probe tip hemisphere for a dc probe for fine-scale structure measurements and the rest of the element for a plasma frequency probe antenna. The spin axis symmetry of the probe systems and freedom from payload doors and mechanisms produced a flight unit that was simple and largely free from rocket wake or spin effects.

In addition to the instruments for electron density measurements, each payload included a magnetic aspect sensor, and an S-band telemetry system including a tone-ranging system.

The rocket systems for boosting the electron density probes were of two types providing different apogee altitudes. The two November 1976 flights (51-3 and 51-4) utilized three-stage rockets composed of Honest John-Nike Hydacs shown in Figure A-2 to achieve altitudes of nearly 500 km. The 1978 flight (51-2) achieved just over 300 km with an Honest John-Hydac.

Details of the electron density probes are given in the following sections.

Plasma Frequency Probe

The plasma frequency probe (PFP) utilizes the well-established relationships between plasma frequency, electron density, and the reactance of a probe immersed in the plasma to provide a measurement

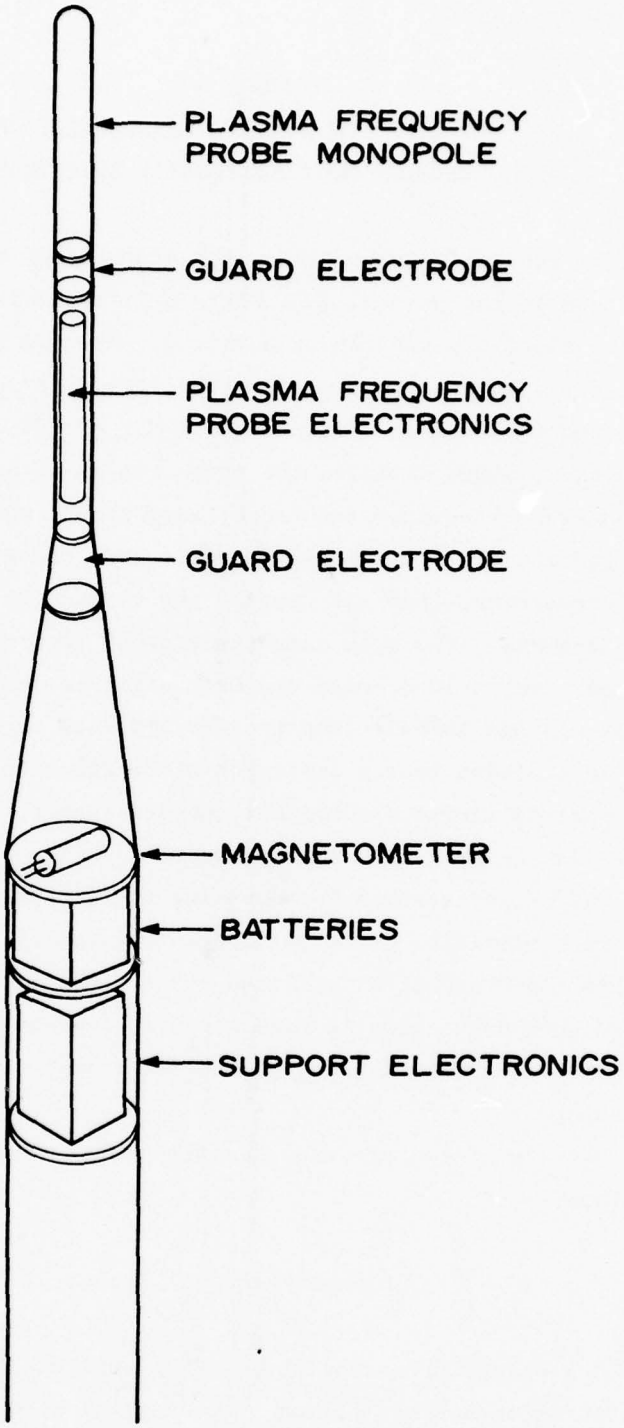

Figure A-1. Probe configuration for auroral wideband satellite support rockets WS614.51-3,-4.

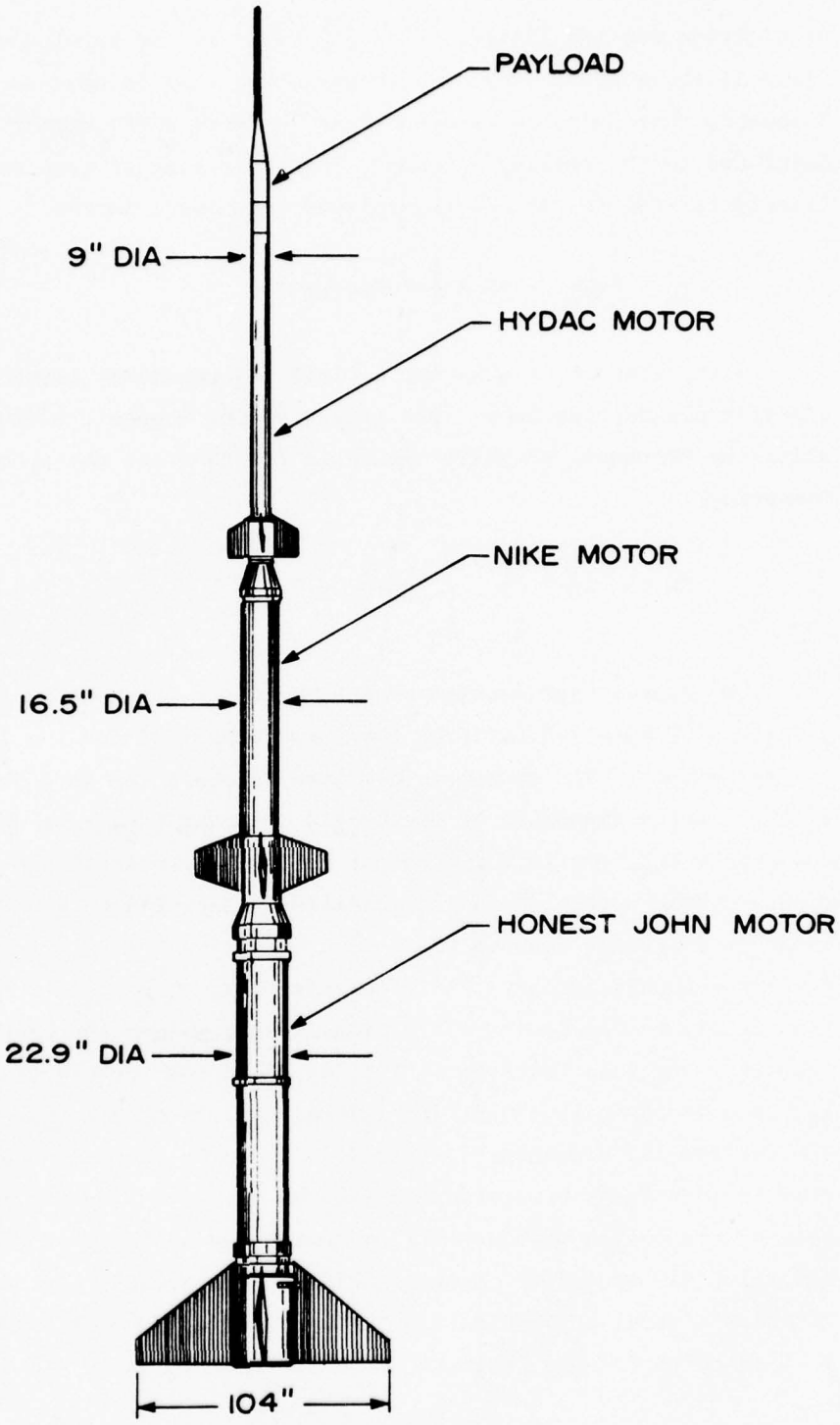

Figure A-2. Honest John - Nike - Hydac Rocket system for electron density measurements.

of electron density [Baker, et al., 1969]. In the version of the PFP flown in the auroral program a phase-locked loop is used to track the frequency that produces zero phase angle between rf current and voltage being fed to the sensing antenna. This frequency of resonance is closely related to the electron plasma frequency, in kHz

$$f_N^2 = \frac{e^2 N_e}{4\pi^2 m_e} = 80.6 \times 10^6 N_e(cm^{-3})$$

In the absence of a magnetic field the resonance occurs at this electron plasma frequency. The effect of the magnetic field is to shift the resonance slightly higher in frequency to the upper hybrid frequency

$$f_H^2 = \sqrt{f_N^2 + f_B^2}\quad , \text{ where } f_B = \frac{eB}{2\pi m_e}$$

The phase-locked version of the PFP which is shown in the block diagram of Figure A-3 utilizes the forward half of the 1-m long nose as its antenna. The system is designed to sense the zero phase condition of the antenna impedance at the hybrid resonant frequency and to cause a phase-locked loop to force the rf oscillator to track the frequency producing the zero phase angle condition. The frequency of the oscillator is digitally counted for 1 msec and forms the data for a digital plasma frequency readout. Additionally, the voltage controlling the loop oscillator is monitored to provide an analog measurement of plasma frequency and loop operation. The digital output provides excellent accuracy in the measurement of electron density at samples with about a meter spatial dimension separated in space by the distance the payload travels in a 16-ms sample period ($\sim$25 m). In order to provide higher spatial resolution measurements, a continuous analog channel and an accoupled x10 amplified channel (ΔPFP) were provided that responded down to about 1 meter scale size fluctuations. The range of electron densities covered by the plasma frequency probe is from about 10^3 to $2 \times 10^6 cm^{-3}$.

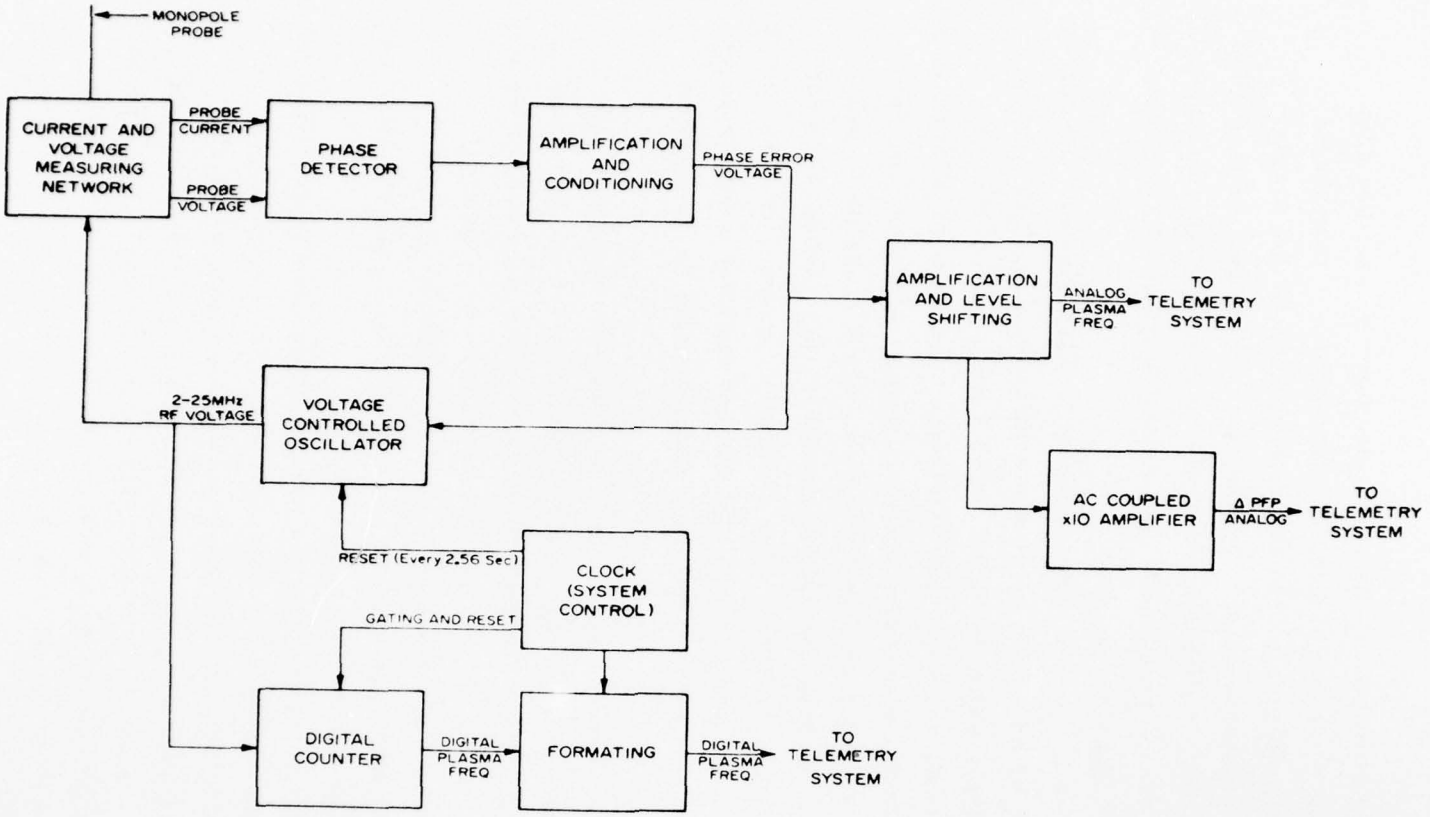

PLASMA FREQUENCY PROBE BLOCK DIAGRAM

Figure A-3. Block diagram of plasma frequency probe.

DC Probe

The DC probe operates on the principle that the electron flow to a small, positively charged electrode immersed in the ionospheric plasma is directly related to the electron density of the plasma. Figure A-4 is a conceptual block diagram of the DC probes used in the auroral program. As its sensing electrode in contact with the ionospheric plasma, the DC probe uses the foremost segment of the payload nose spike with dimensions as noted.

The operation of the DC probe is exceptionally simple. The current collected by the 63 cm^2 probe electrode (the forward 4.76 cm of the payload nose spike), which is biased at +3 V with respect to the rest of the payload, is fed to the electronics system preamplifier at B. With a finite sensing electrode current caused by electron flow from the plasma to the electrode, the voltages at C and D are not equal, and the differential stage amplifies the difference giving an output which is proportional to the sensing electrode current flow. The output from the differential amplifier is fed to four amplifiers having gains of x1, x10, x100, and x1000 with the four outputs going to the payload telemetry section.

The DC probes used in the auroral program were designed to be capable of measuring fine-scale spatial variations of electron density. This high spatial resolution capability is determined by the dimension of the probe electrode, the payload velocity, and the electrical bandwidth of the telemetry system. For these applications the telemetry system bandwidth and the payload velocity limit the DC probe spatial resolution to the order of 50 cm.

The DC probe current cannot be related independently to electron density with high absolute accuracy, but will give reliable relative values. This does not present a serious drawback here since the relative changes $\Delta N_e/N_e$ are the important values and over a limited altitude range the electron density will be proportional to the probe current. By cross comparison to other measurements such as the rf probe or an ionosonde, the DC probe can be calibrated in absolute numbers.

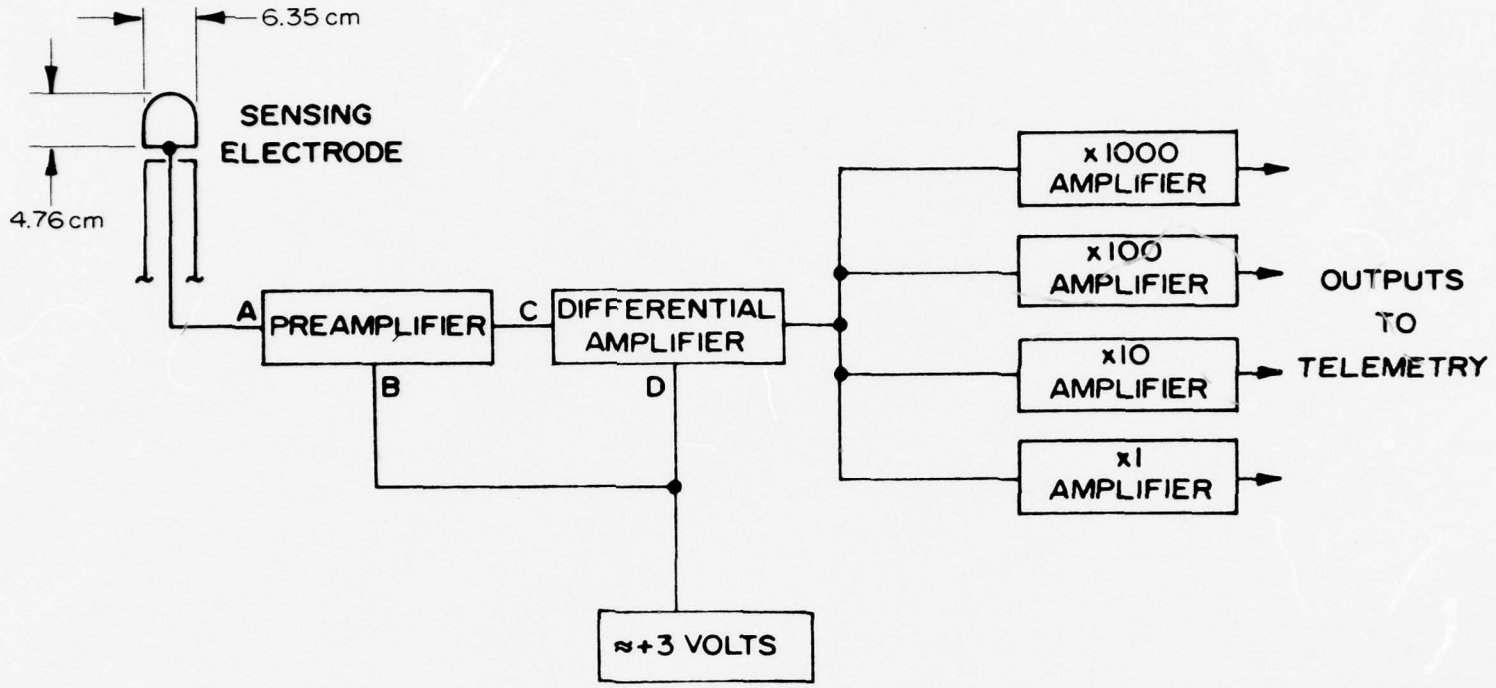

DC PROBE BLOCK DIAGRAM

Figure A-4. Block diagram of DC probe.

APPENDIX B

PRELIMINARY RESULTS FROM DAYTIME EVENT OF 1 MARCH 1978

For comparison with the earlier results, the preliminary results from the March 1978 daytime flight are included here. Honest John-Hydac WS 810.51-2 was launched at 1906 UT (0906 local time) on 1 March 1978 in conjunction with the daytime pass of the DNA Wideband satellite. The quick-look results were presented to DNA as a field report which is hereby appended for reference. In addition, a more refined set of electron density profiles from the rocket flight are presented in Figures B-1 and B-2.

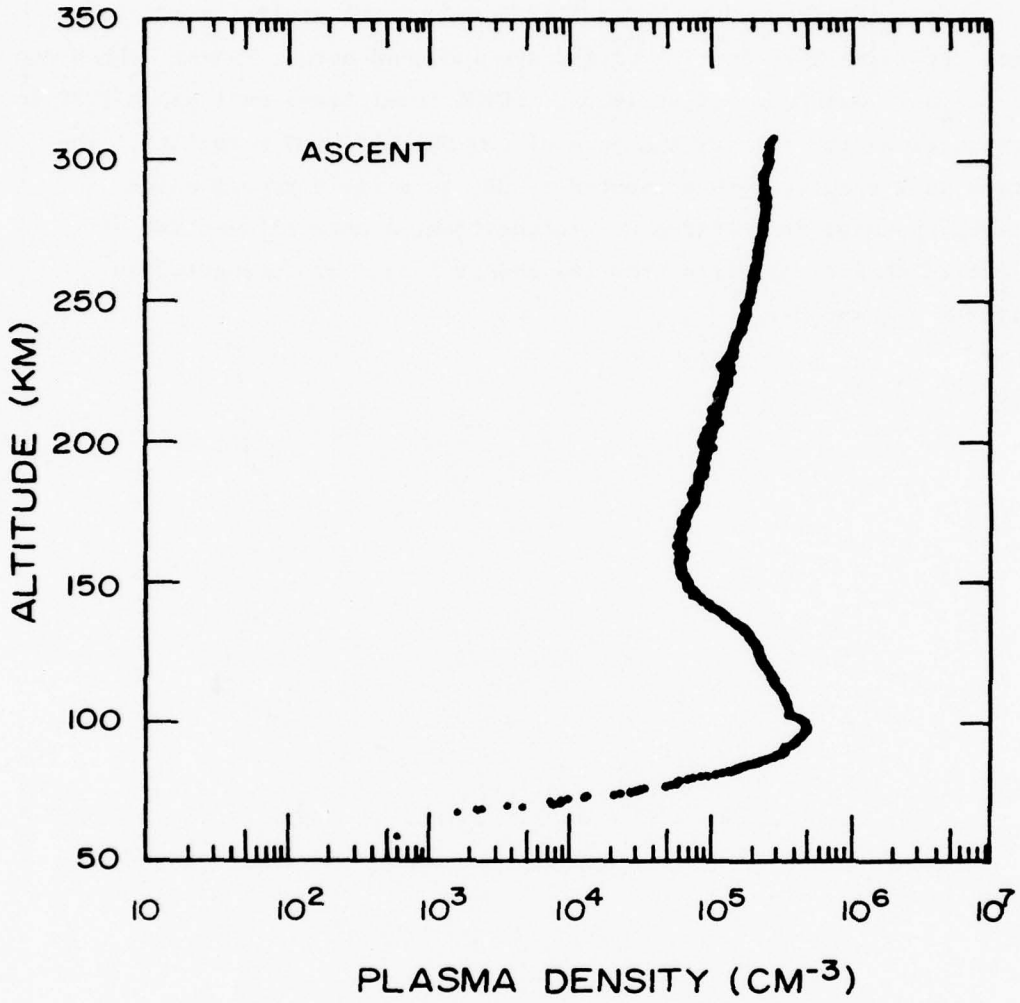

Figure B-1. Electron density derived from DC probe measurements aboard profile WS614.51-2 for ascent. (B-1)

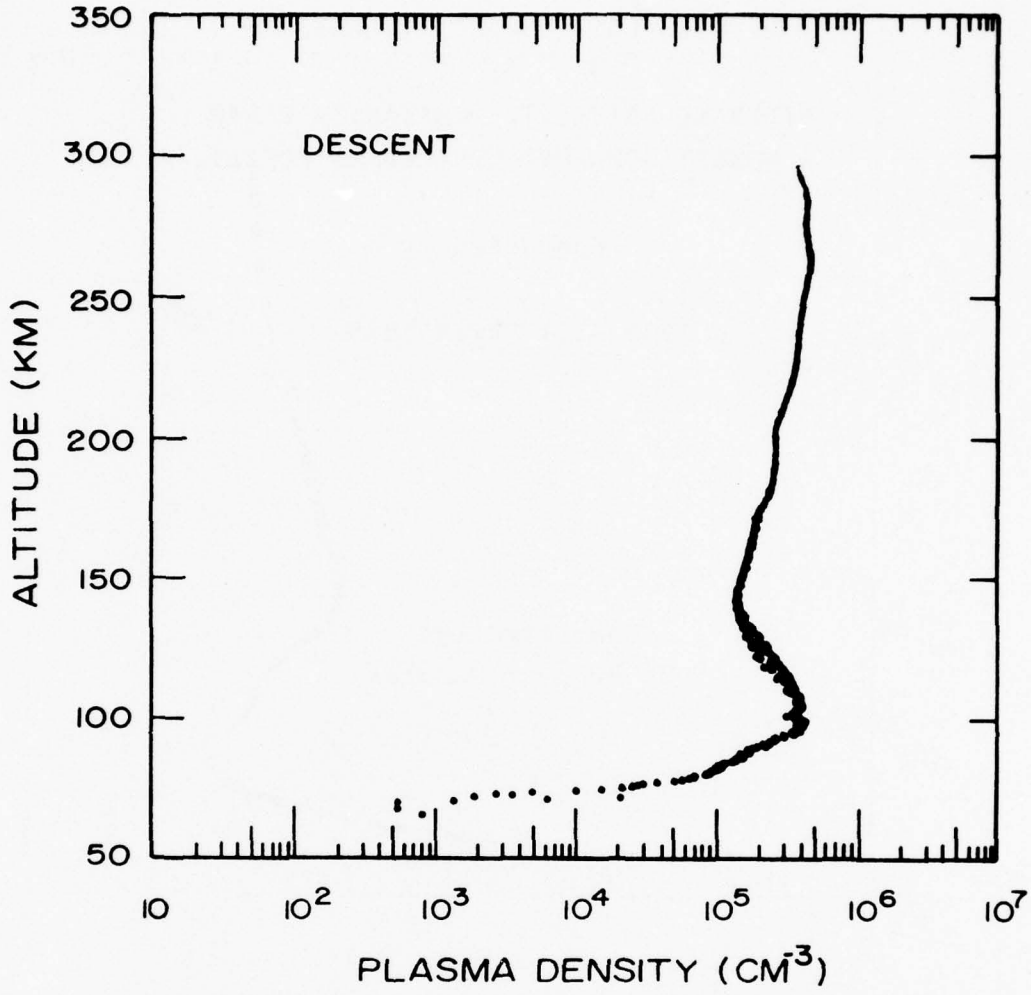

Figure B-2. Electron density derived from DC probe measurements aboard profile WS614.51-2 for descent. (B-2)

FIELD REPORT OF
COORDINATED DAYTIME INVESTIGATION
OF HIGH LATITUDE SCINTILLATIONS
BY
WIDEBAND SATELLITE, CHATANIKA RADAR
& HONEST JOHN-HYDAC WIDEBAND ROCKET

Conducted

1906 UT 1 March 1978

Submitted to:
DNA Program Manager

by:

Air Force Geophysics Laboratories
SRI International
and
Utah State University

SUMMARY

The Wideband probe rocket was launched on 1 March 1978 during a daytime pass (0906 a.m. Alaska Standard Time) of the Wideband Satellite. Supporting measurements were provided by the Chatanika incoherent scatter radar, the Homer auroral clutter radar, and the magnetometers and riometers at Poker Flat and Fort Yukon.

Scintillation activity was stronger during this launch than during any of the previous three Wideband probe launches (all previous launches took place near midnight). Moderate (5 - 10 db) to strong (10 - 20 db) VHF scintillation was present throughout the pass as is becoming typical for morning passes following a strong magnetic disturbance during the night.

In contrast to previous launches, a well developed F-region, with deep valley between the E- and F-layers was present during the pass. The E-layer at 95 km was produced by moderately intense precipitation of rather hard auroral particles; the F-layer by solar EUV. The DC probe currents show dramatic (~10%) variations in electron density at altitudes between 150 and 300 km; i.e., on the relatively steep bottomside gradient of the F-layer.

1. INTRODUCTION & LAUNCH SITUATION

On 1 March 1978 at 1906 UT (0906 local time) an instrumented Honest John-Hydac rocket was launched from the Poker Flat Rocket Range, Alaska coordinated with the overpass of the SRI/DNA Wideband Satellite to provide the first daytime altitude profile and structure of electron density simultaneous with strong scintillations on the satellite transmissions recorded at the Wideband receiving site at Poker Flat. The Chatanika incoherent scatter radar was measuring the ambient ionospheric conditions in the vicinity of the satellite transmission path and rocket trajectory to provide simultaneous electron density contour maps and electric field information. In addition, the auroral clutter radar at Homer, Alaska operated during the mission, and information was obtained about auroral activity and the energy deposition region over a widespread area around Poker Flat. Figure 1.1 shows a sketch of the principle experiments at Poker Flat involved in the mission and the general geometry of the rocket launches. The rocket flight aximuth was approximately 20° east of the magnetic meridian. The magnetic field is from the south (the B-field arrow in the sketch) at an inclination of approximately 77°. The disturbed atmospheric region through which the rocket probed and the satellite transmissions propogated is shown in the sketch (auroral region).

The Wideband receiving site recorded moderate to strong scintillations throughout the overpass of the satellite. The track of the line-of-site E-region (110 km) and F-region (350 km) penetrations are shown in Figure 1.2. Also shown is nominal rocket launch aximuth. The rocket trajectory (preliminary) is shown in Figure 1.3. The rocket upleg passed close to the satellite E-region penetration track. The Chatanika radar (as shown in Figure 1.1 by the 110 km

E-region scan) at satellite pass time changed from a magnetic meridian scan to a scan azimuth nearly parallel to the satellite track.

Since this experiment was performed in daylight, there was no optical coverage of the aurora. During the previous evening there was a great deal of auroral activity with two very bright breakups. The magnetometer was active throughout the night and into the daylight hours. This was one of the criteria for launch readiness since the Poker Flat Wideband data showed a history of strong scintillations when similar situations occurred. Figure 1.4 shows a portion of the Ft. Yukon magnetometer record around launch time. Note the previous activity and that the rocket was launched during a negative deviation of about 300 gammas. The Poker Flat riometer, operating at 30 MHz, showed an absorption event at the time of launch indicative of very energetic particles being deposited in the upper atmosphere. Figure 1.5 shows the riometer record at and after launch. The final criteria for launch was, of course, real-time observation of the strong scintillations at the Wideband receiving site.

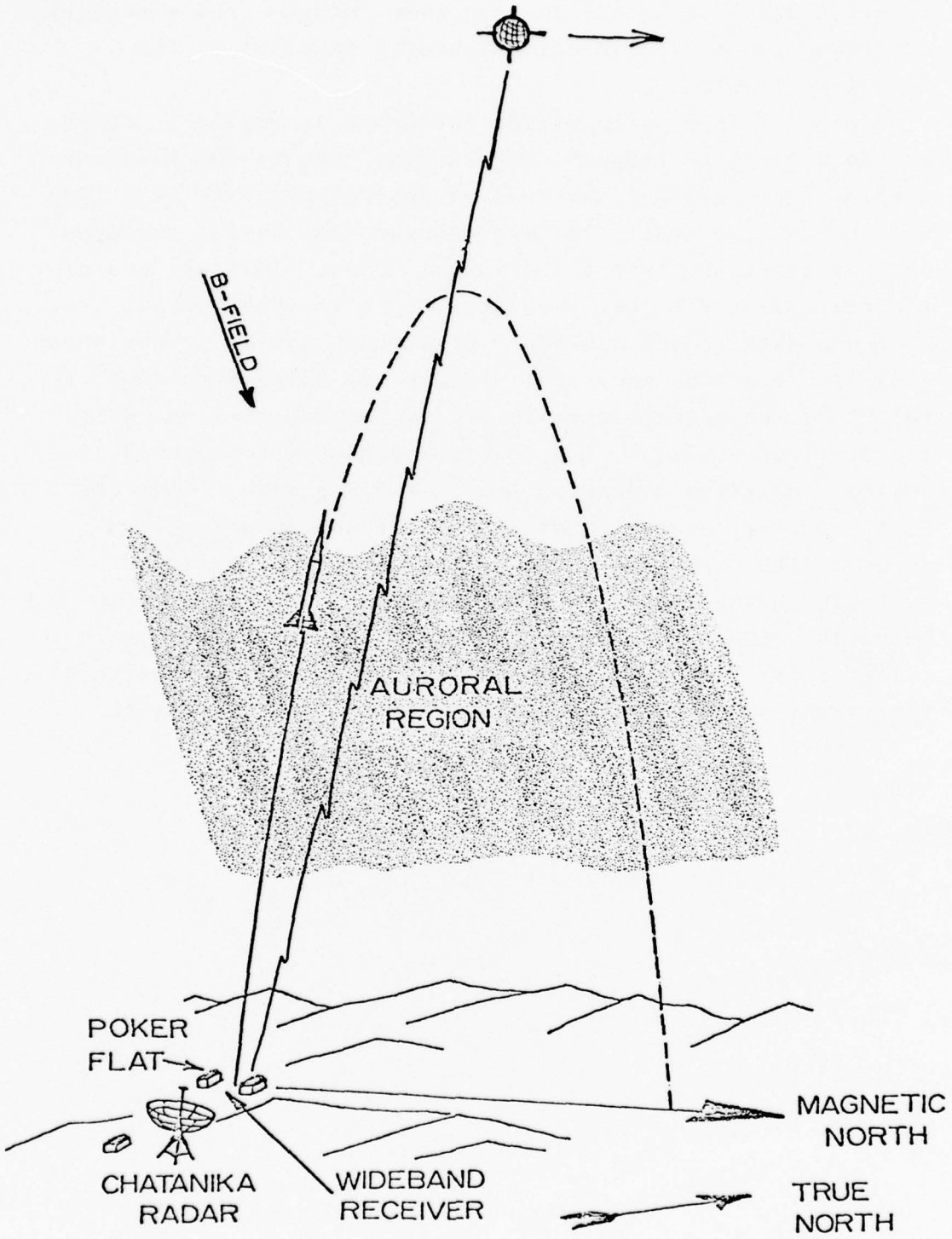

Figure 1.1. Sketch of the principle experiments involved in the wideband auroral experiment and the general geometry of the rocket launch.

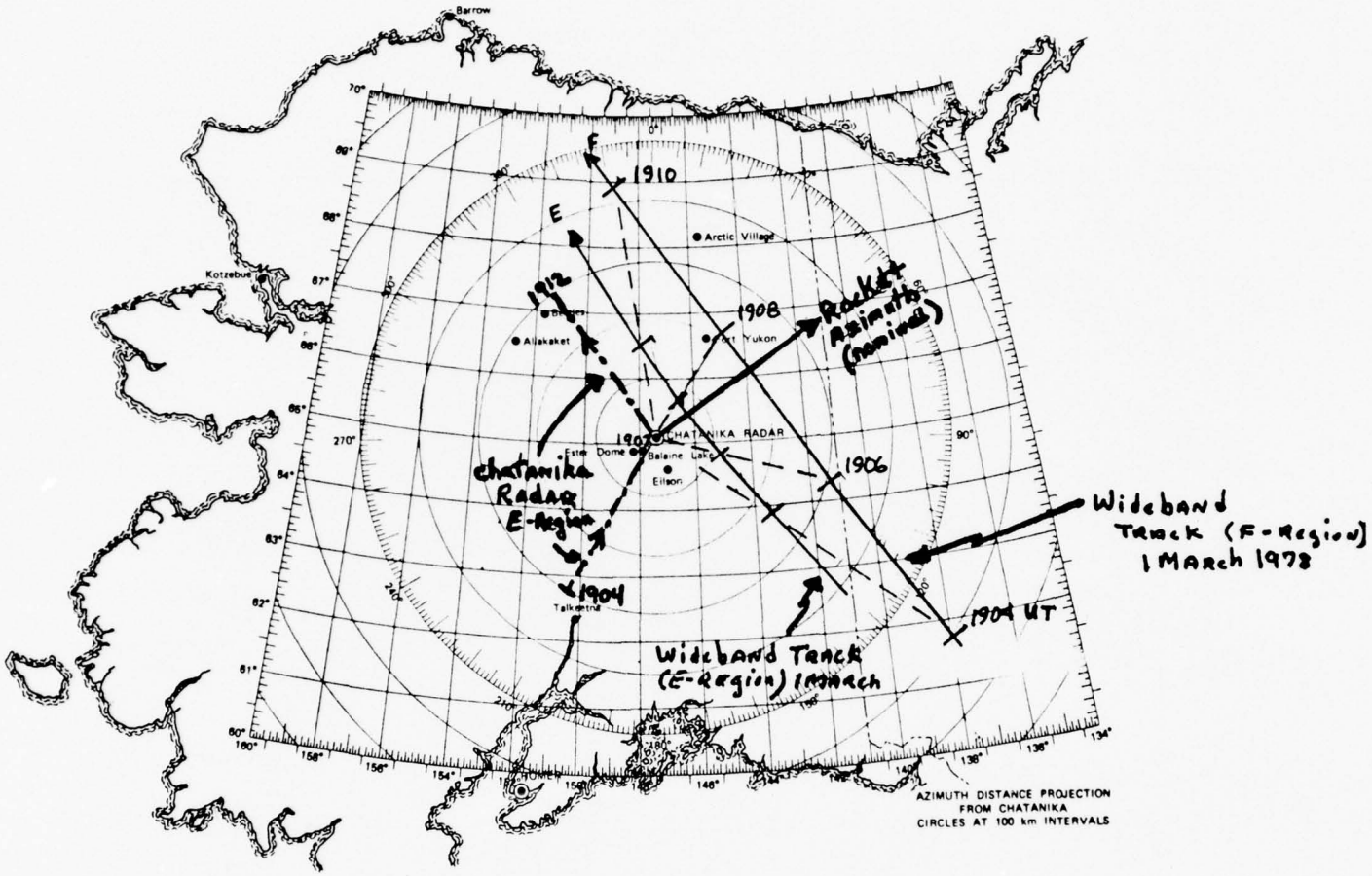

Figure 1.2. The track of the line-of-site E-region (110 km) and F-region (350 km) penetrations, the rocket flight azimuth and the E-region (110 km) penetration location of the Chatanika radar scan.

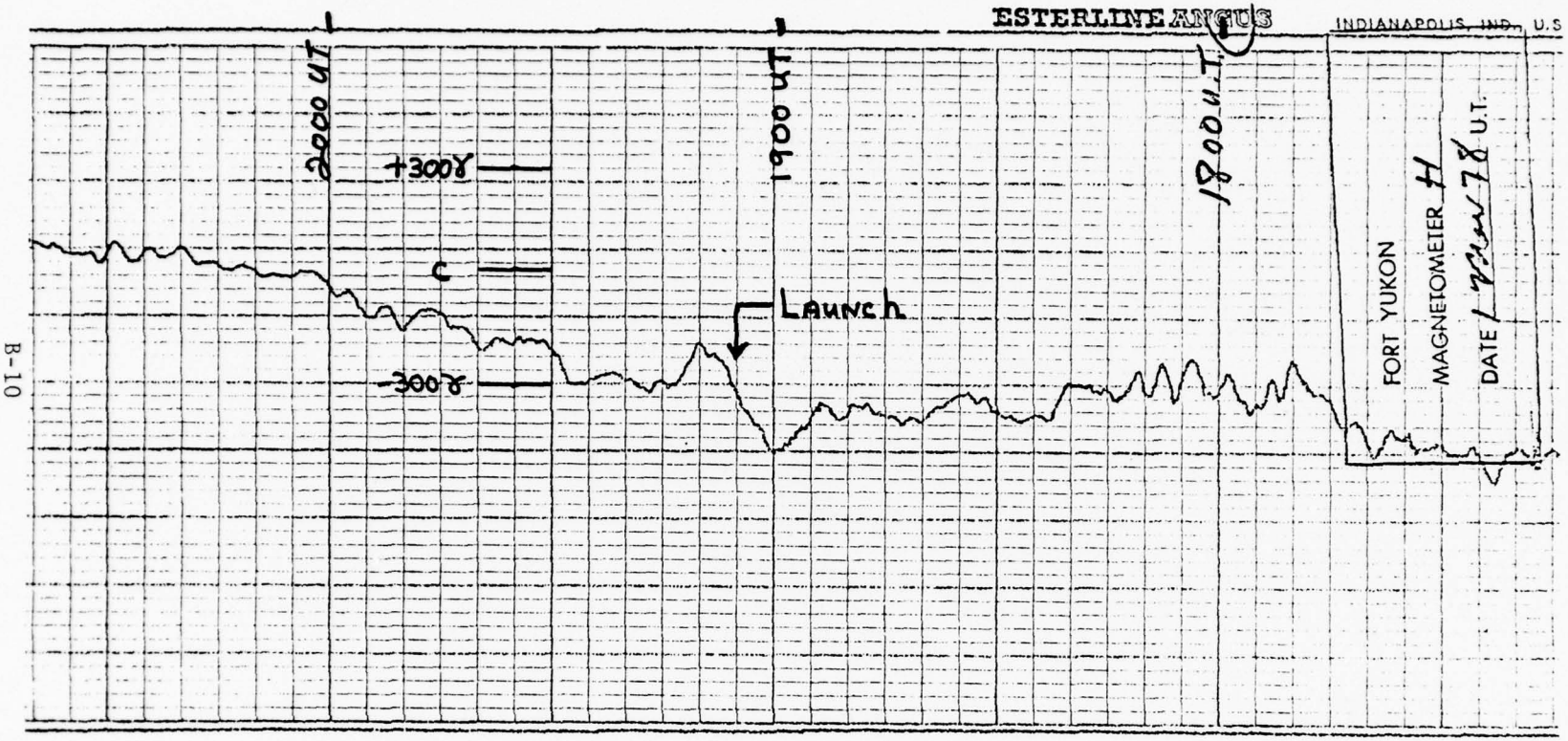

Figure 1.3. The H magnetometer record at Fort Yukon around launch time of the wideband rocket and overpass of the satellite indicating strong magnetic activity.

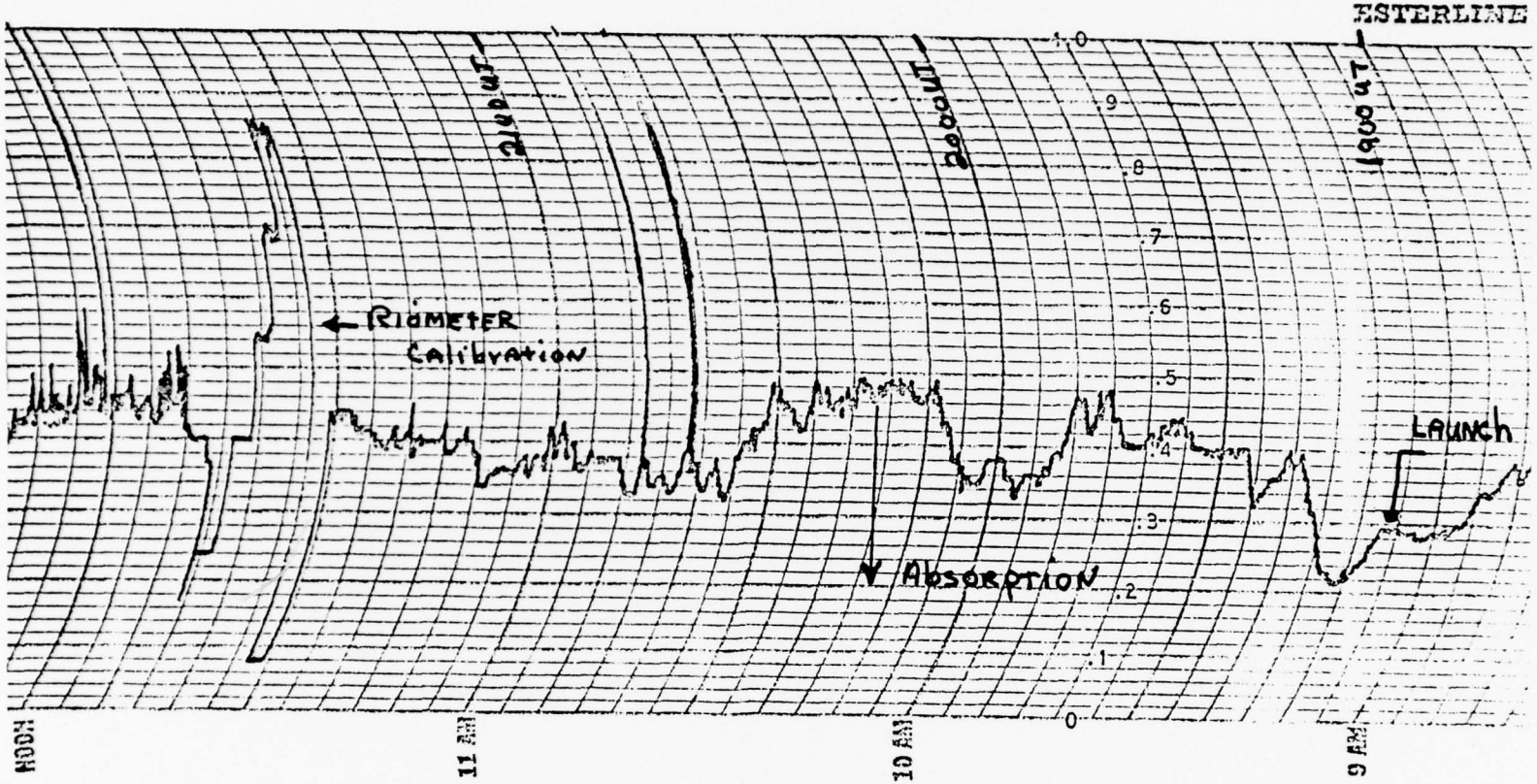

Figure 1.4. The College riometer record showing an absorption event in progress at the launch of the wideband rocket and during the overpass of the satellite.

2. WIDEBAND SATELLITE AND CHATANIKA RADAR RESULTS

Wideband Satellite

The detrended VHF (137 MHz) wideband amplitude and phase records are shown in Figure 2.1. Scintillation well in excess of 10 dB can be seen during several portions of the pass. Another interesting feature is the change in the temporal character of the amplitude signal near 1905 UT. Before that time the fading rate is appreciably slower than afterwards. The change in temporal structure probably indicates a change in either irregularity altitude or irregularity drift between the regions probed before and after 1905 UT.

The first-order statistical analysis results at VHF and UHF (413 MHz) for this pass are shown in Figures 2.2 and 2.3. At VHF, S_4 was of order 0.6 to 0.7 for much of the pass and the rms phase variance (σ_ϕ) was of order 3 radians. At UHF, S_4 was between 0.1 and 0.2 and the phase variance was of order 1 radian. There is no apparent change in either S_4 or σ_ϕ associated with the change in temporal structure at 1905 UT.

Spectral analysis of the multifrequency Wideband data is underway which will ultimately provide a valuable comparison between the irregularity spectrum measured by the satellite and the in-site spectrum measured by the rocket probe.

Chatanika Radar

The Chatanika radar operated in an elevation scan mode from 1747 to 2108 UT in support of the Wideband rocket. The scans covered the region from 15° above the northern horizon to 15° above the southern horizon. Scans were made in the magnetic meridian until near satellite pass time when the scan azimuth was aligned nearly parallel to the satellite track (see Figure 1.2).

From the processed radar data, electron density as a function of height and distance, and electric fields, currents, and energy deposition (all as functions of horizontal distance) will be derivable.

Quick-look data reduction was performed in the field. Figure 2.4 shows a representative electron density profile obtained just prior to the Wideband satellite pass. A substantial E-region existed with a peak density of 3.3×10^5 el/cm^3 at 95 km. Above the E-layer was an F-layer peaking at about 300 km with a maximum density of about 2×10^5 el/cm^3. Between the E-and F-layers was an ionization minimum at about 150 km.

The electron density varied spatially as can be seen from Figure 2.5, a contour map of electron density in the meridian plane. This map was made between 1857 and 1905, just prior to rocket launch. An E-layer density enhancement can be seen to the north as well as the valley between the E- and F-layers. F-layer densities above about 250 km and through the layer peak were not available in time for this report.

A preliminary interpretation of the electric field data indicates the presence of a south-eastward component of about 10 mv/m.

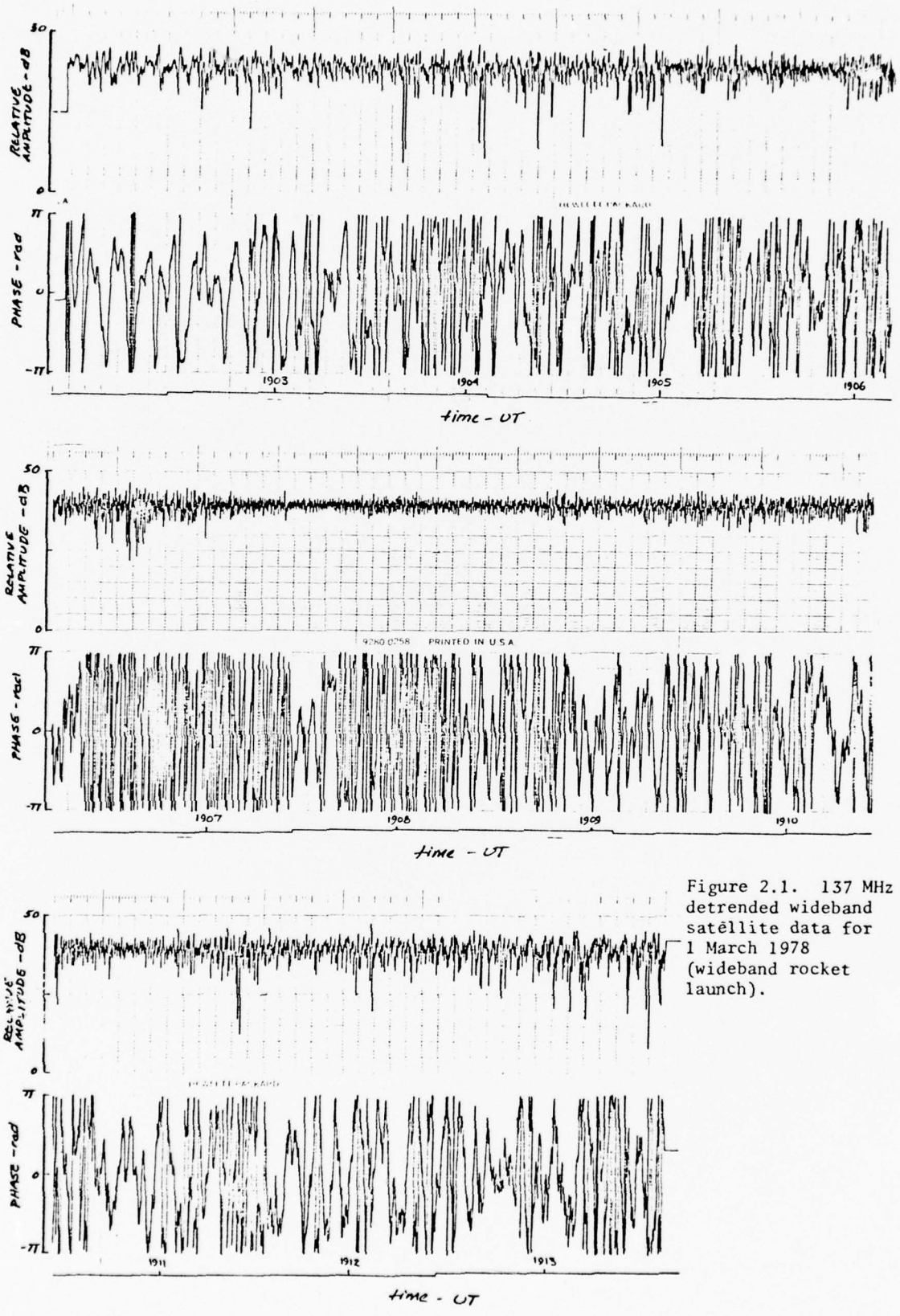

Figure 2.1. 137 MHz detrended wideband satellite data for 1 March 1978 (wideband rocket launch).

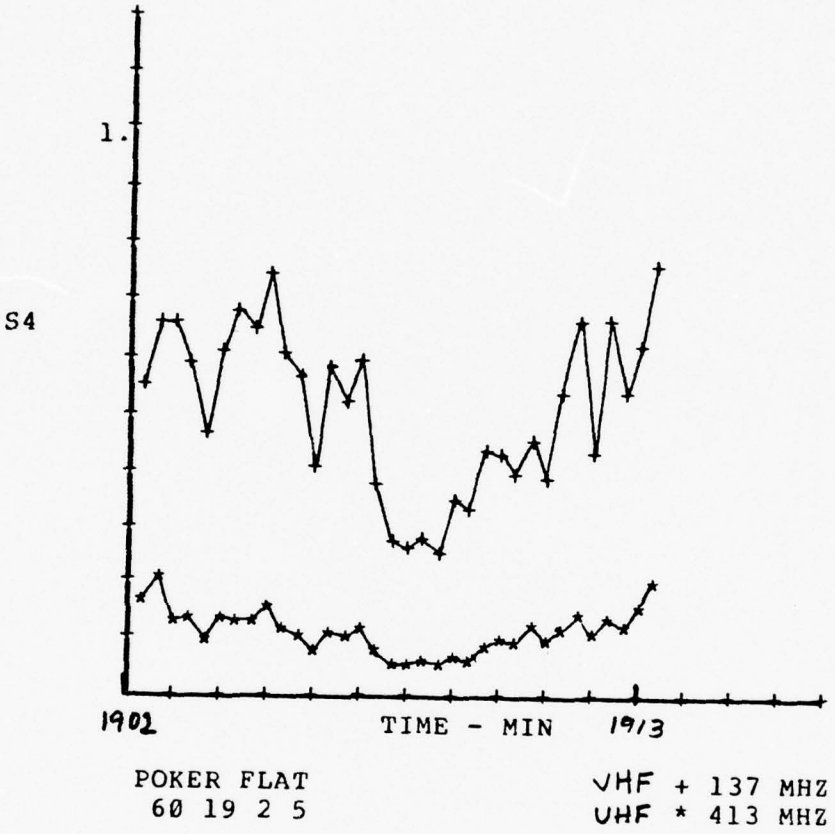

Figure 2.2. Wideband satellite: S_4 Index at VHF and UHF.

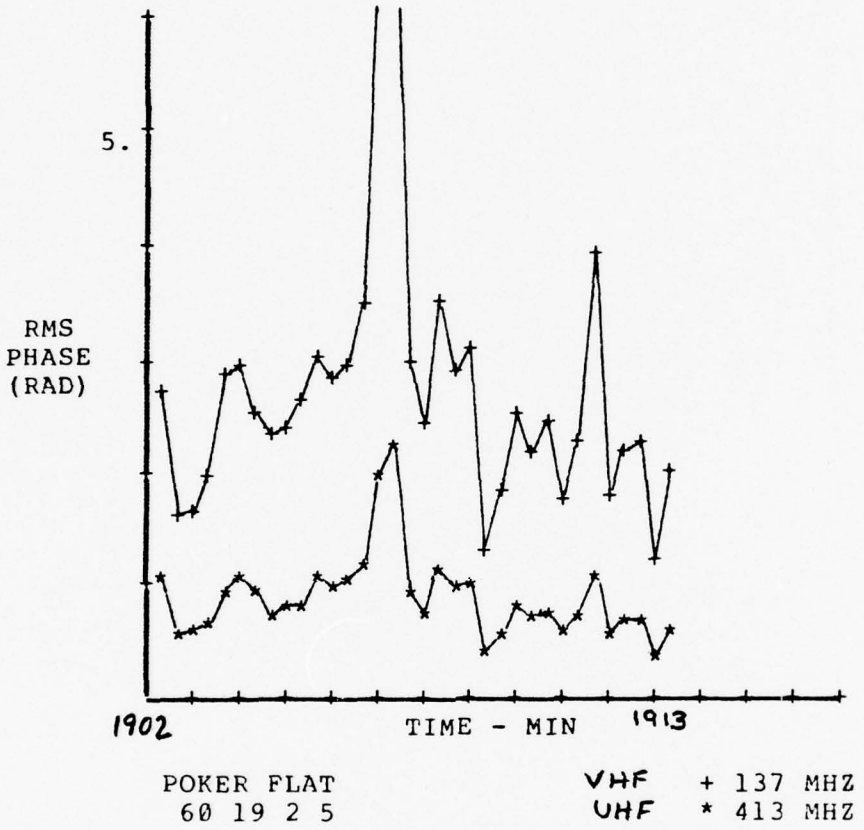

Figure 2.3. Wideband satellite: RMS phase at VHF and UHF.

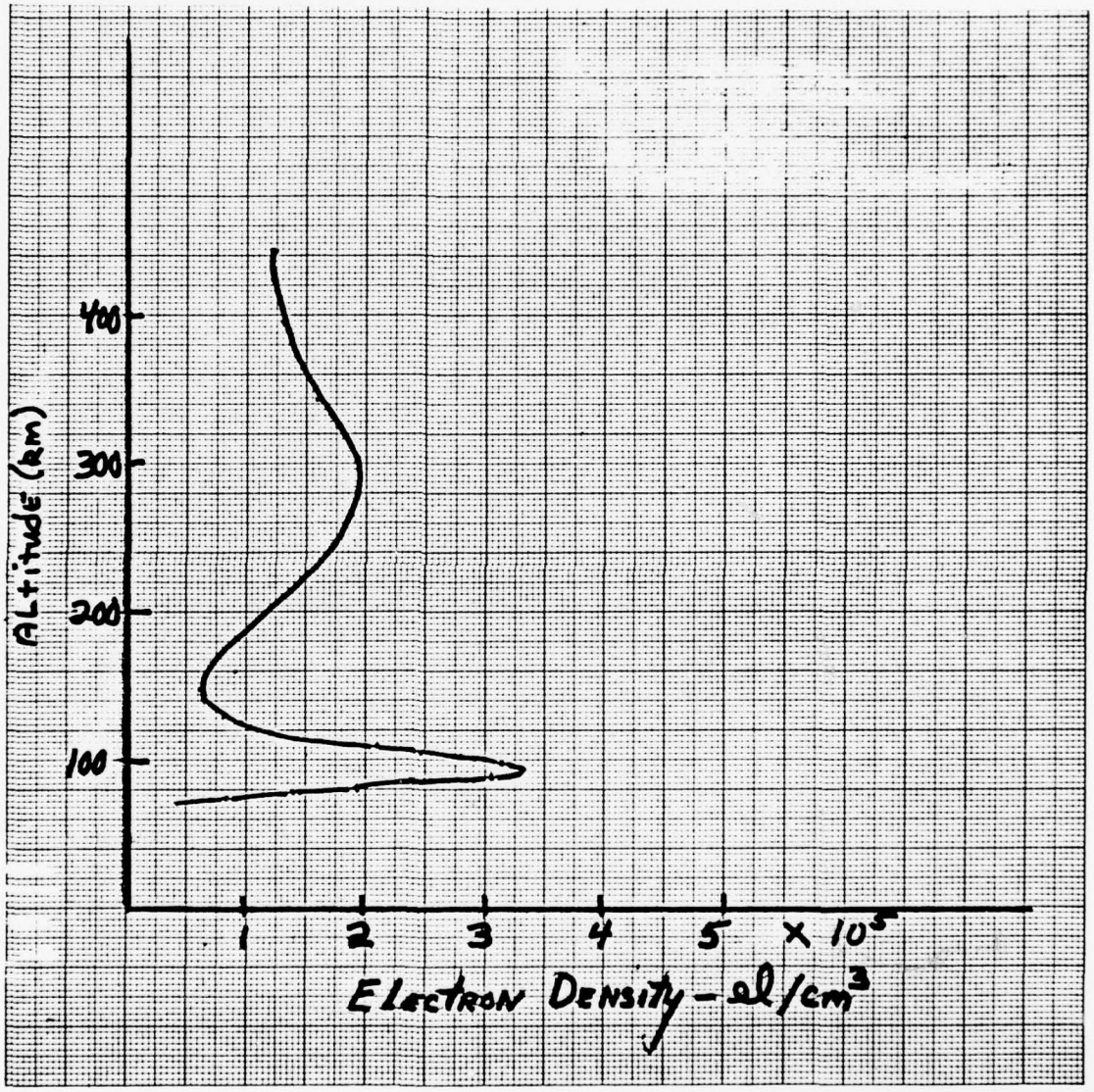

Figure 2.4. Electron density profile from Chatanika radar results 1 March 1978 (1902:38 - 1902:53 UT).

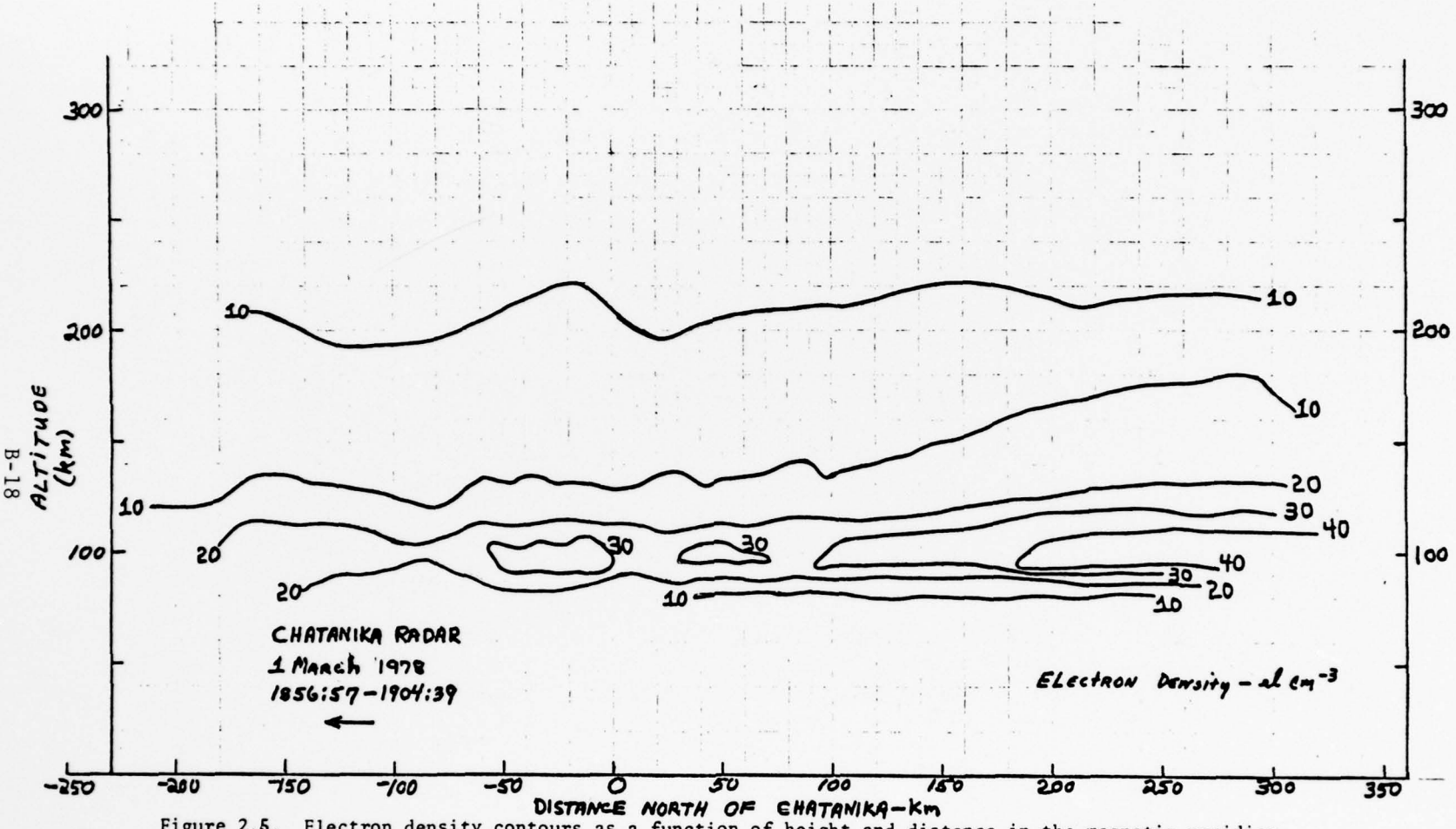

Figure 2.5. Electron density contours as a function of height and distance in the magnetic meridian (wideband rocket launch).

3. ROCKET PROBE MEASUREMENTS

The payload of the Honest John-Hydac rocket WS810.51-2 for auroral Wideband Satellite support measurements consisted of a combination DC and RF plasma frequency probe for measurement of electron density and its fine scale structure. Each of these probes utilized a portion of the 1-meter nose spike for the sensing element. The instrument and telemetry bandwidths were large enough to allow probe current variations (and hence electron density variations) to be measured with spatial resolution better than one meter. The DC probe using this electrode with spin axis symmetry gives clean and reliable relative electron density structure but cannot be related independently to the absolute electron concentration with high accuracy. The absolute densities can be obtained accurately with the plasma frequency probe. This probe measures the electron plasma frequency by locking an RF oscillator onto the frequency that produces a zero phase angle between the RF current and voltage on the nose spike antenna. The combined use of these two probes provides electron density measurement with both high accuracy and high spatial resolution.

Honest John-Hydac WS810.51-2 was launched at 1906:00 1 March 1978 in conjunction with the overpass of the Wideband satellite. The rocket flight was close to nominal and all probes, telemetry tracking and other systems performed normally.

The electron density profiles measured by the plasma frequency probe are shown in Figure 3.1 for rocket ascent and Figure 3.2 for descent. The layer at about 90 km with a peak density of about 5×10^5 cm^{-3} verifies that moderately intense precipitation of rather hard auroral particles was occurring during the rocket flight. Above this layer the density drops off by almost an order of magnitude to a deep valley at 150 km. Above the valley, the F-region density

increases to about 1.5×10^5 at rocket apogee of 307 km. The F-region density on the descent profile is considerably greater with a broad maximum that appears to be the F-region peak at about 270 km. The valley at 150 km is not as pronounced on this profile as it was on rocket ascent. The 90 km layer however is nearly the same as shown earlier.

The probe current from the DC probe for rocket ascent and descent are shown in Figures 3.3 and 3.4 respectively. The probe current shows dramatic spatial structure over the regions indicated on the ascent profile. The variations in density of these structures are on the order of 10% over the regions indicated.

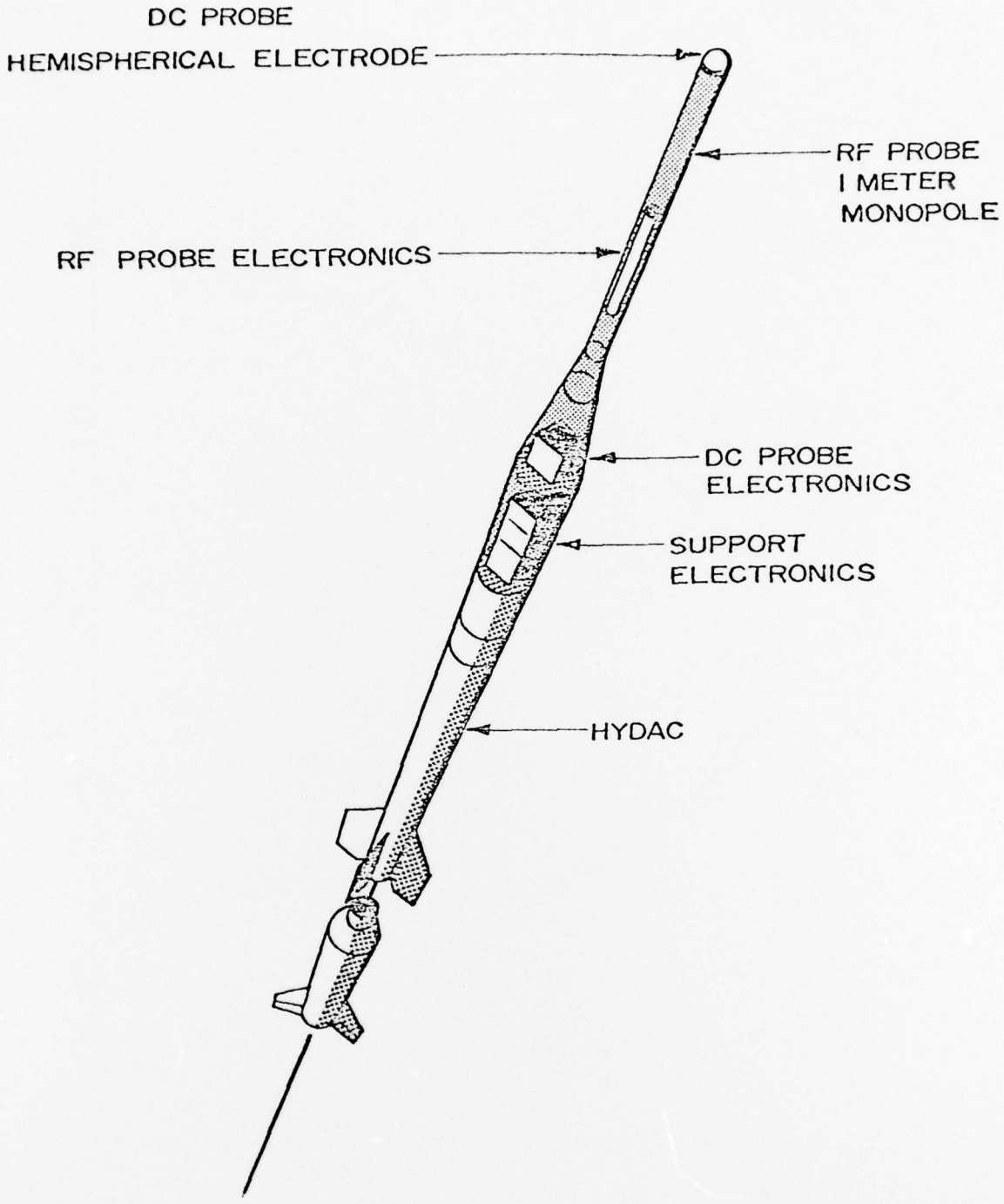

Figure 3.1. Rocket probe for wideband auroral program.

WS810.51-2

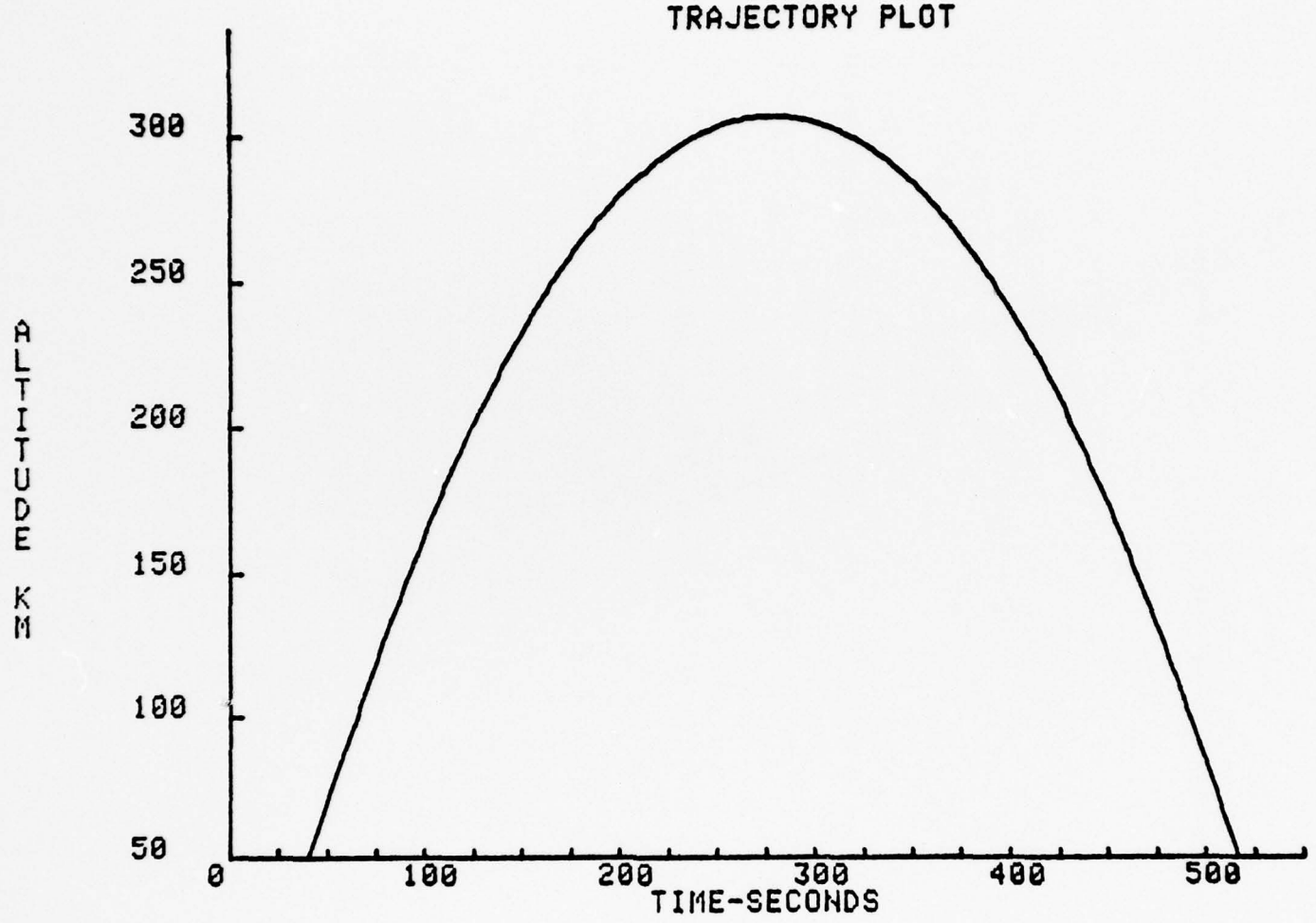
TRAJECTORY PLOT
ALTITUDE KM
300
250
200
150
100
50
0
100
200
300
400
500
TIME-SECONDS

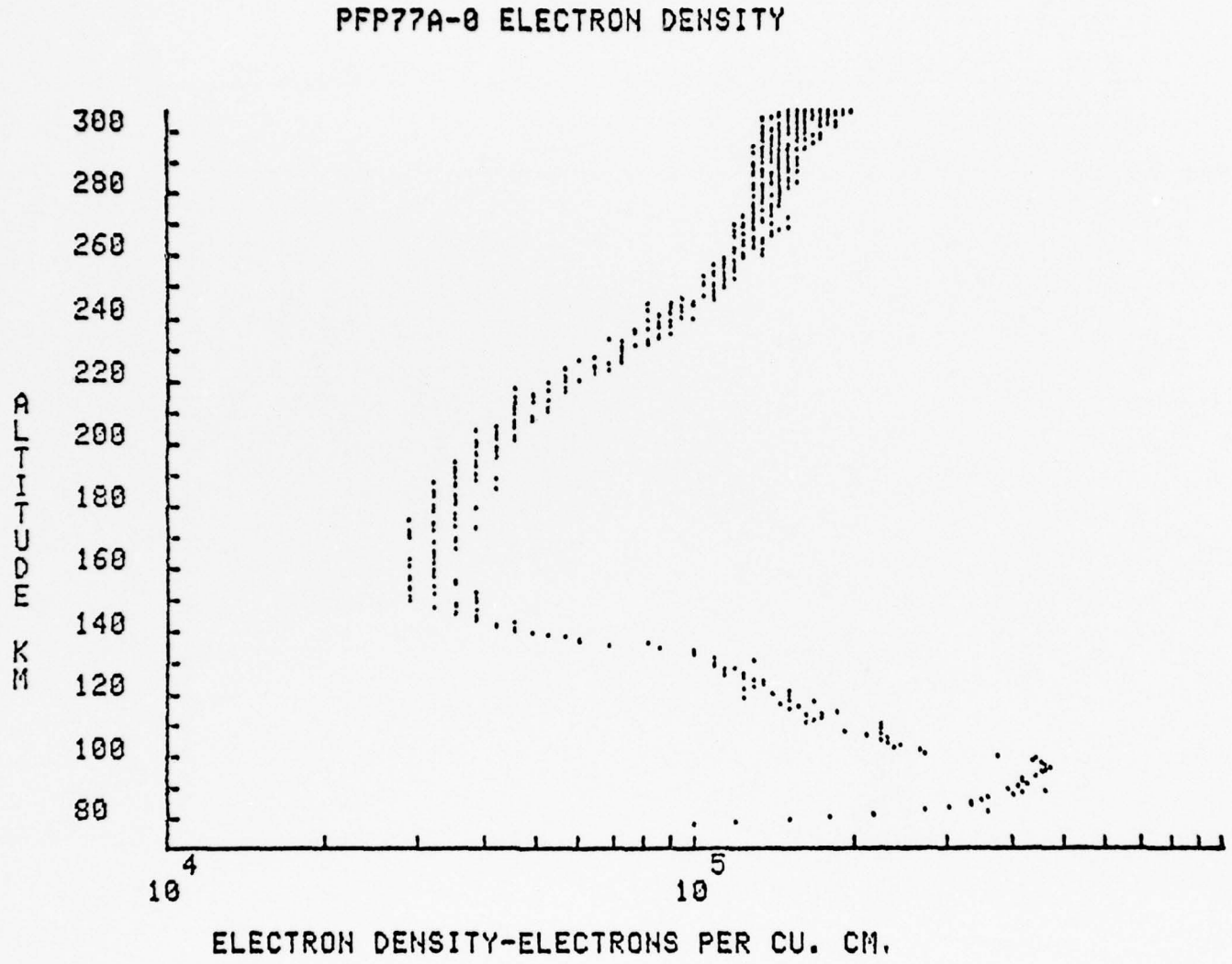

Figure 3.3. Electron density profile (Ascent) from plasma frequency probe - WS 810.51-2.

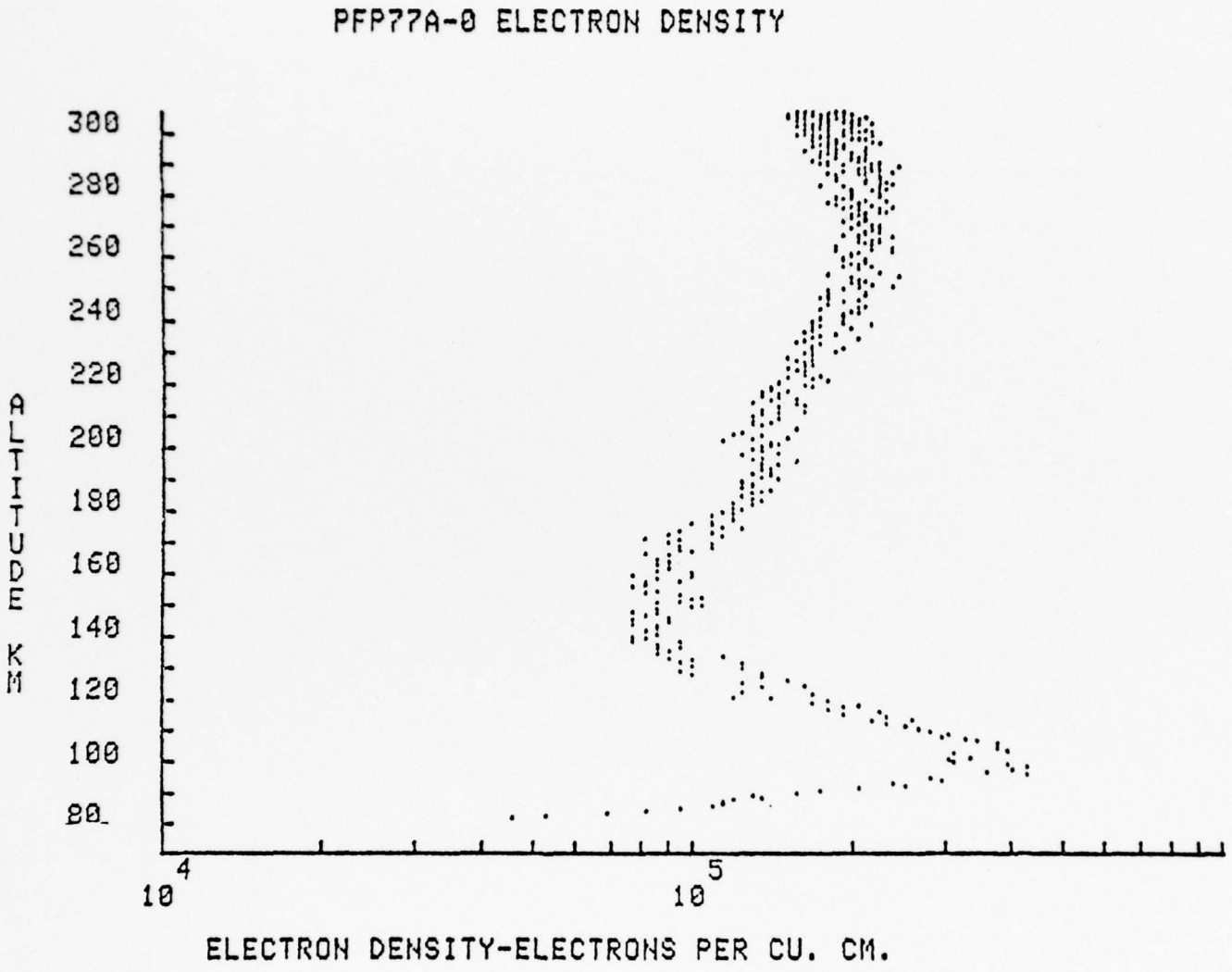

Figure 3.4. Electron density profile (Descent) from plasma frequency probe - WS 810.51-2.

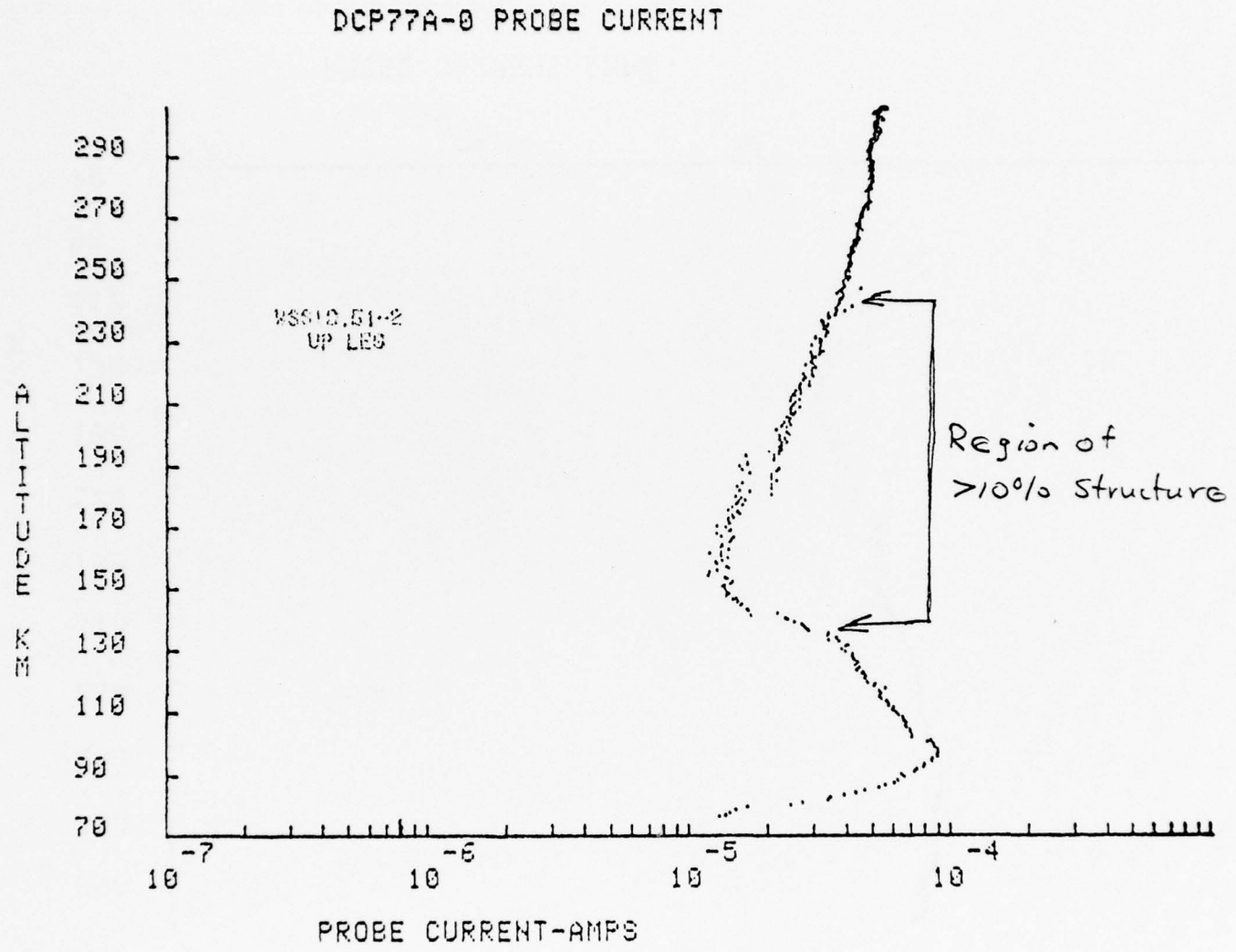

Figure 3.5. DC Probe current (Ascent) - WS 810.51-2.

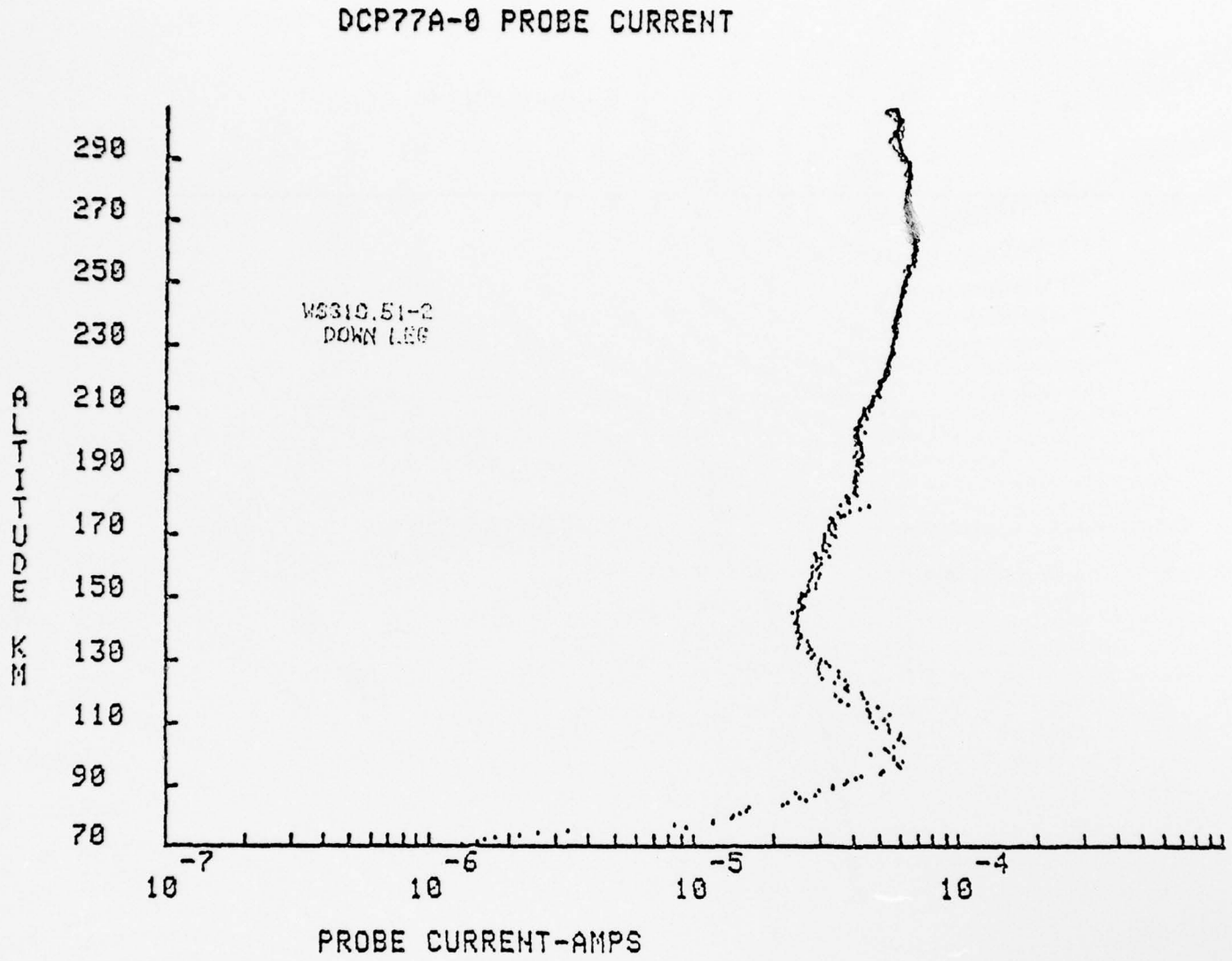

Figure 3.6. DC Probe current (Descent) - WS 810.51-2.

DISTRIBUTION LIST

DEPARTMENT OF DEFENSE

Assistant Secretary of Defense
Comm, Cmd, Cont. & Intell.
ATTN: M. Epstein
ATTN: J. Babcock

Assistant to the Secretary of Defense
Atomic Energy
ATTN: Executive Assistant

Command & Control Technical Center
Department of Defense
ATTN: C-312, R. Mason
ATTN: C-650, G. Jones
ATTN: C-650, W. Heidig

Defense Advanced Rsch. Proj. Agency
ATTN: TIO

Defense Communications Agency
ATTN: Code 480
ATTN: 101B
ATTN: Code 810, J. Barna
ATTN: Code R1033, M. Raffensperger

Defense Communications Engineer Center
ATTN: Code R720, J. Worthington
ATTN: Code R410, J. McLean

Defense Documentation Center
12 cy ATTN: DD

Defense Intelligence Agency
ATTN: DC-7D, W. Wittig
ATTN: DB-4C, E. O'Farrell
ATTN: HQ-TR, J. Stewart
ATTN: DB, A. Wise
ATTN: DT-5
ATTN: DT-1BZ, R. Morton
ATTN: DT-1B

Defense Nuclear Agency
ATTN: DDST
ATTN: STVL
3 cy ATTN: RAAE
4 cy ATTN: TITL

Field Command,
Defense Nuclear Agency
ATTN: FCPR

Field Command
Defense Nuclear Agency
Livermore Division
ATTN: FCPRL

Interservice Nuclear Weapons School
ATTN: TTV

Joint Chiefs of Staff
ATTN: J-3, WWMCCS Evaluation Office
ATTN: J-37

Joint Strat. Tgt. Planning Staff
ATTN: JLTW-2
ATTN: JPST, G. Goetz

DEPARTMENT OF DEFENSE (Continued)

National Security Agency
Department of Defense
ATTN: R52, J. Skillman
ATTN: B3, F. Leonard
ATTN: W32, O. Bartlett

Under Secretary of Defense for Rsch. & Engrg.
ATTN: Strategic & Space Systems (OS)

WWMCCS System Engineering Org.
ATTN: R. Crawford
ATTN: T. Neighbors

DEPARTMENT OF THE ARMY

Atmospheric Sciences Laboratory
U.S. Army Electronics R & D Command
ATTN: DELAS-AD-M, F. Niles

BMD Systems Command
Department of the Army
2 cy ATTN: BMDSC-HW

Deputy Chief of Staff for Ops. & Plans
Department of the Army
ATTN: DAMO-TCZ, P. Kenny
ATTN: DAMO-TCW

Electronics Tech. & Devices Lab.
U.S. Army Electronics R & D Command
ATTN: DELET-ER, *H. Bomke*

Harry Diamond Laboratories
Department of the Army
ATTN: DELHD-N-P
ATTN: DELHD-N-RB, R. Williams
ATTN: DELHD-N-P, F. Wimenitz
ATTN: DELHD-N-TL, M. Weiner

U. S. Army Comm-Elec. Engrg. Instal. Agency
ATTN: CCC-EMEO, W. Nair
ATTN: CCC-EMEO, PED, G. Lane

U.S. Army Foreign Science & Tech. Center
ATTN: DRXST-SD

U.S. Army Materiel Dev. & Readiness Command
ATTN: DRCLDC, J. Bender

U.S. Army Nuclear & Chemical Agency
ATTN: Library

U.S. Army Satellite Comm. Agency
ATTN: Document Control

U.S. Army TRADOC Systems Analysis Activity
ATTN: ATAA-PL
ATTN: ATAA-TCC, F. Payan, Jr.
ATTN: ATAA-TDC, J. Hesse

U.S. Army Communications Command
ATTN: CC-OPS-WR, H. Wilson

DEPARTMENT OF THE NAVY

Joint Cruise Missile Project Office
Department of the Navy
ATTN: JCM-G-70

Naval Air Development Center
ATTN: Code 6091, M. Setz

Naval Electronic Systems Command
ATTN: NAVELEX 3101, T. Hughes
ATTN: PME 117
ATTN: Code 501A
ATTN: PME 117-T
ATTN: PME 106-13, T. Griffin
ATTN: PME 106-4, S. Kearney

Naval Intelligence Support Center
ATTN: NISC-50

Naval Ocean Systems Center
ATTN: Code 532, J. Bickel
ATTN: M. Paulson
ATTN: Code 8151, C. Baggett
3 cy ATTN: Code 5324, W. Moler

Naval Research Laboratory
ATTN: Code 7580
ATTN: Code 7555
ATTN: Code 6700, T. Coffey
ATTN: Code 6707, J. Davis
ATTN: Code 7500, B. Wald
ATTN: Code 6701, J. Brown

Naval Space Surveillance System
ATTN: J. Burton

Naval Surface Weapons Center
ATTN: Code F-14, R. Butler

Naval Surface Weapons Center
White Oak Laboratory
ATTN: Code F31

Naval Telecommunications Command
ATTN: Code 341

Office of Naval Research
ATTN: Code 420
ATTN: Code 421

Office of the Chief of Naval Operations
ATTN: OP-604
ATTN: OP-941D
ATTN: OP-981N

Strategic Systems Project Office
Department of the Navy
ATTN: NSSP-2722, F. Wimberly
ATTN: NSP-2141

DEPARTMENT OF THE AIR FORCE

Aerospace Defense Command
Department of the Air Force
ATTN: DC, Mr. Long

DEPARTMENT OF THE AIR FORCE (Continued)

Aerospace Defense Command/XPD
Department of the Air Force
ATTN: XPDQ
ATTN: XP

Air Force Avionics Laboratory
ATTN: AAD, W. Hunt
ATTN: AAD, A. Johnson

Air Force Geophysics Laboratory
ATTN: LKB, K. Champion
ATTN: OPR-1, J. Ulwick
ATTN: PHP, J. Aarons
ATTN: PHI, J. Buchau
ATTN: PHP, J. Mullen
ATTN: OPR, A. Stair

Air Force Weapons Laboratory
ATTN: DYC, J. Barry
ATTN: SUL
ATTN: DYC, J. Frasier

Air Logistics Command
Department of the Air Force
ATTN: OO-ALC/MM, R. Blackburn

Assistant Chief of Staff
Intelligence
Department of the Air Force
ATTN: INED

Deputy Chief of Staff
Operations, Plans & Readiness
Department of the Air Force
ATTN: AFXOXFD
ATTN: AFXOKCD
ATTN: AFXOKT
ATTN: AFXOKS

Deputy Chief of Staff
Research, Development, & Acq.
Department of the Air Force
ATTN: AFRDQ
ATTN: AFRDSP
ATTN: AFRDSS
ATTN: AFRDS

Assistant Chief of Staff
Studies and Analyses
Department of the Air Force
ATTN: AF/SASC, R. Paul
ATTN: AF/SASC

Electronic Systems Division, AFSC
ATTN: DCKC, J. Clark
ATTN: XRW, J. Deas
ATTN: YSEA
ATTN: YSM, J. Kobelski

Foreign Technology Division, AFSC
ATTN: TQTD, B. Ballard
ATTN: NIIS, Library

Rome Air Development Center, AFSC
ATTN: V. Coyne, OCS
ATTN: TSLD

DEPARTMENT OF THE AIR FORCE (Continued)

Rome Air Development Center, AFSC
ATTN: EEP

Space & Missile Systems Organization
Air Force Systems Command
ATTN: MNNL, S. Kennedy

Space & Missile Systems Organization
Air Force Systems Command
ATTN: SKA, M. Clavin
ATTN: SKA, C. Rightmyer

Space & Missile Systems Organization
Air Force Systems Command
ATTN: SZJ, L. Doan

Strategic Air Command
Department of the Air Force
ATTN: XPFS
ATTN: NRT
ATTN: DCX
ATTN: OOKSN
ATTN: DCXF
ATTN: DCXT

DEPARTMENT OF ENERGY

Albuquerque Operations Office
ATTN: D. Sherwood

Department of Energy
ATTN: Doc. Con. for A. Labowitz

DEPARTMENT OF ENERGY CONTRACTORS

Lawrence Livermore Laboratory
University of California
ATTN: Technical Information Department Library

Los Alamos Scientific Laboratory
ATTN: P. Keaton
ATTN: D. Westervelt
ATTN: R. Taschek

Sandia Laboratories
ATTN: W. Brown
ATTN: D. Dahlgren
ATTN: D. Thornbrough
ATTN: 3141
ATTN: Space Projects Division

Sandia Laboratories
Livermore Laboratory
ATTN: B. Murphy
ATTN: T. Cook

OTHER GOVERNMENT AGENCIES

Central Intelligence Agency
ATTN: OSI/PSTD, Rm. 5, F 19

Department of Commerce
National Bureau of Standards
ATTN: R. Moore

Department of Commerce
National Oceanic & Atmospheric Admin.
ATTN: R. Grubb
ATTN: G. Reid

OTHER GOVERNMENT AGENCIES (Continued)

Department of Transportation
Office of the Secretary
ATTN: R. Lewis
ATTN: R. Doherty

Institute for Telecommunications Sciences
National Telecommunications & Info. Admin.
ATTN: L. Berry
ATTN: A. Jean
ATTN: W. Utlaut
ATTN: D. Crombie

U.S. Coast Guard
Department of Transportation
ATTN: G-DOE-3/TP54, B. Romine

DEPARTMENT OF DEFENSE CONTRACTORS

Aerospace Corp.
ATTN: F. Morse
ATTN: N. Stockwell
ATTN: I. Garfunkel
ATTN: D. Olsen
ATTN: S. Bower
ATTN: J. Carter
ATTN: T. Salmi
ATTN: R. Slaughter
ATTN: V. Josephson

Analytical Systems Engineering Corp.
ATTN: Radio Sciences

BDM Corp.
ATTN: L. Jacobs

Berkeley Research Associates, Inc.
ATTN: J. Workman

Boeing Co.
ATTN: J. Kenney
ATTN: D. Murray
ATTN: G. Hall
ATTN: S. Tashird

BR Communications
ATTN: J. McLaughlin

University of California at San Diego
ATTN: H. Booker

Charles Stark Draper Lab., Inc.
ATTN: D. Cox
ATTN: J. Gilmore

Computer Sciences Corp.
ATTN: H. Blank

Comsat Labs.
ATTN: G. Hyde
ATTN: R. Taur

Cornell University
Department of Electrical Engineering
ATTN: D. Farley, Jr.

Electrospace Systems, Inc.
ATTN: H. Logston

DEPARTMENT OF DEFENSE CONTRACTORS (Continued)

ESL, Inc.
ATTN: C. Prettie
ATTN: J. Roberts
ATTN: J. Marshall

Ford Aerospace & Communications Corp.
ATTN: J. Mattingley

General Electric Co.
Space Division
ATTN: M. Bortner

General Electric Co.
ATTN: F. Reibert

General Electric Company-TEMPO
Center for Advanced Studies
ATTN: W. Knapp
ATTN: M. Stanton
ATTN: T. Stevens
ATTN: D. Chandler
ATTN: DASIAC

General Electric Tech. Services Co., Inc.
HMES
ATTN: G. Millman

General Research Corp.
Santa Barbara Division
ATTN: J. Ise, Jr.
ATTN: J. Garbarino

Geophysical Institute
University of Alaska
ATTN: N. Brown
ATTN: T. Davis
ATTN: Technical Library

GTE Sylvania, Inc.
Electronics Systems Grp.-Eastern Div.
ATTN: M. Cross

HSS, Inc.
ATTN: D. Hansen

IBM Corp.
Federal Systems Division
ATTN: F. Ricci

University of Illinois
Department of Electrical Engineering
ATTN: K. Yeh

Institute for Defense Analyses
ATTN: E. Bauer
ATTN: J. Aein
ATTN: J. Bengston
ATTN: H. Wolfhard

International Tel. & Telegraph Corp.
ATTN: Technical Library

JAYCOR
ATTN: S. Goldman

Kaman Sciences Corp
ATTN: T. Meagher

DEPARTMENT OF DEFENSE CONTRACTORS (Continued)

Johns Hopkins University
Applied Physics Lab.
ATTN: T. Potemra
ATTN: Document Librarian
ATTN: P. Komiske
ATTN: T. Evans
ATTN: J. Newland
ATTN: B. Wise

Linkabit Corp.
ATTN: I. Jacobs

Litton Systems, Inc.
Amecom Division
ATTN: R. Grasty

Lockheed Missiles & Space Co., Inc.
ATTN: Dept. 60-12
ATTN: D. Churchill

Lockheed Missiles and Space Co., Inc.
ATTN: R. Johnson
ATTN: M. Walt
ATTN: W. Imhof

M.I.T. Lincoln Lab.
ATTN: D. Towle
ATTN: L. Loughlin

McDonnell Douglas Corp.
ATTN: N. Harris
ATTN: G. Mroz
ATTN: J. Moule
ATTN: W. Olson

Mission Research Corp.
ATTN: R. Hendrick
ATTN: S. Gutsche
ATTN: F. Fajen
ATTN: D. Sowle
ATTN: R. Bogusch
ATTN: M. Scheibe

Mitre Corp.
ATTN: C. Callahan
ATTN: G. Harding
ATTN: A. Kymmel

Mitre Corp.
ATTN: W. Foster
ATTN: M. Horrocks
ATTN: W. Hall

Pacific-Sierra Research Corp.
ATTN: E. Field, Jr.

Pennsylvania State University
Ionosphere Research Lab.
ATTN: Ionospheric Research Lab.

Photometrics, Inc.
ATTN: I. Kofsky

Physical Dynamics, Inc.
ATTN: E. Fremouw

DEPARTMENT OF DEFENSE CONTRACTORS (Continued)

R & D Associates
ATTN: R. Lelevier
ATTN: B. Gabbard
ATTN: R. Turco
ATTN: F. Gilmore
ATTN: H. Ory
ATTN: W. Karzas
ATTN: W. Wright, Jr.
ATTN: C. MacDonald
ATTN: C. Greifinger
ATTN: M. Gantsweg

Rand Corp.
ATTN: E. Bedrozian
ATTN: C. Crain

Riverside Research Institute
ATTN: V. Trapani

Science Applications, Inc.
ATTN: L. Linson
ATTN: D. Hamlin
ATTN: D. Sachs
ATTN: F. Straker
ATTN: J. McDougall
ATTN: C. Smith

Science Applications, Inc.
Huntsville Division
ATTN: D. Divis

Science Applications, Inc.
ATTN: SZ

Rockwell International Corp.
Collins Telecommunications Sys. Division
ATTN: J. Kristof

DEPARTMENT OF DEFENSE CONTRACTORS (Continued)

SRI International
ATTN: G. Carpenter
ATTN: C. Rino
ATTN: G. Smith
ATTN: G. Price
ATTN: R. Leadabrand
ATTN: W. Jaye
ATTN: W. Chesnut
ATTN: M. Baron
ATTN: A. Burns
ATTN: D. Neilson
ATTN: R. Livingston

Teledyne Brown Engineering
ATTN: R. Deliberis

Tri-Com, Inc.
ATTN: D. Murray

TRW Defense & Space Sys. Group
ATTN: S. Altschuler
ATTN: R. Plebuch
ATTN: D. Dee

Utah State University
Contract/Grant Office
ATTN: L. Jensen
ATTN: K. Baker
ATTN: J. Ulwick
ATTN: M. Kelley
ATTN: L. Howlett
ATTN: N. Grossbard

Visidyne, Inc.
ATTN: J. Carpenter